Problems of Planetology, Cosmochemistry and Meteoritica

Alexeev V.A. The possible reason of the overestimation of cosmic-ray exposure ages of the Sweden fossil meteorites

Vernadsky Institute of Geochemistry and Analytical Chemistry RAS, Moscow AVAL37@chgnet.ru

Overestimate of the cosmic-ray exposure ages of fossil meteorites of Sweden can be caused by foreign neon with high content of ^{21}Ne.

Key words: [fossil meteorites, cosmic-ray exposure age]

Citation: Alexeev, V. A. (2012), The possible reason of the overestimation of cosmic-ray exposure ages of the Sweden fossil meteorites, Vestnik ONZ RAN, 4, (doi:)1

The parent asteroid of L-chondrites has catastrophically broken up in the asteroid belt at about 500 Ma. The fact that this event caused the delivery of the asteroid's fragments to the Earth soon after its destruction was confirmed by the unusually large occurrence of fossil meteorites in marine limestone of mid-Ordovician in southern Sweden [*Schmitz et al*., *1997; Heck et al., 2004*].

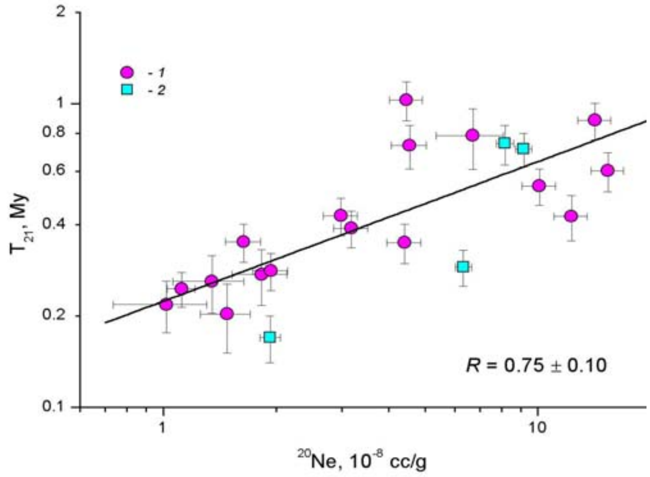

Fig. 1. Values of the exposure age (T_{21}) of fossil meteorites depending on the content of ^{20}Ne in the samples of chromite grains. 1 – meteorites of the non-Ark group [*Alexeev*, *2010*]; 2 – samples of the Brunflo meteorite. A straight line is regression line. (According to *Heck et al.* [*2004, 2008*]; *Heck* [*2005*].)

Heck et al. [*2004, 2008*] measured the contents of noble gases in the chromite grains recovered from these meteorites and calculated their exposure ages (T_{21}). From the analysis of these data, *Alexeev* [*2010*] found that the values of the exposure ages calculated from ^{21}Ne by *Heck et al*. [*2004, 2008*] linearly depend on a mass of grain samples in *logarithmic coordinates.* At the same time, the values of T_{21} linearly depend on the ^{20}Ne contents (Fig. 1). Hereafter, the equation parameters of the regression lines were calculated by Williamson's method [*Williamson*, *1968; Alexeev, 2000*] taking into account the errors of both coordinates. It is essential to note, that this dependence is shown not only for set of samples of different meteorites, but also for samples of s meteorite (Brunflo).

Alexeev [*2010*] suggested that the increase in the concentration of ^{21}Ne and the corresponding values of T_{21} observed for the decreasing mass (M) of samples (sizes of grains) could be caused by the contribution of nucleogenic ^{21}Ne ignored in the calculations of T_{21}. However, the results of measurements of the content of noble gases in the individual chromite grains of terrestrial origin performed by *Meier et al.* [*2010*] put into question the validity of the explanation of the obtained dependence of T_{21} on M suggested by *Alexeev* [*2010*], but did not explain the nature of this dependence. Below, the possible explanation of the found dependence is discussed.

We have compared dependences of the content of ^{21}Ne vs. ^{20}Ne in the chromite grains of a terrestrial origin and in the grains separated from fossil meteorites (Fig. 2). The equation parameters of the regression lines are given in the Table. The parameter b = 0.00283 ± 0.00088 for chromite grains of a terrestrial origin, within the limits of a statistical error, coincides with value of the $^{21}Ne/^{20}Ne_{atm}$ ratio for an atmosphere (0.00298). However, parameter b = 0.0084 ± 0.0005 for meteorite grains is significantly above the $^{21}Ne/^{20}Ne_{atm}$ value.

The found anomalous dependence of the ^{21}Ne content on ^{20}Ne content can be explained by the presence of gases of terrestrial origin in the admixtures that were not completely removed from the cracks and cavities in the chromite grains of meteorites. The enriching of neon by isotope of ^{21}Ne in the gas of these admixtures (when the ratio $^{21}Ne/^{20}Ne_{adm} >> ^{21}Ne/^{20}Ne_{atm}$) will cause the contribution of ^{21}Ne ignored in calculations of the cosmogenic $^{21}Ne_{cos}$ content. The value of this contribution and the corresponding values of T_{21} will increase with decreasing sizes and preservation degree of the recovered grains. Such enrichment can be real, since the data obtained by *Verkhovskii et al.* [*1976*] for terrestrial rocks showed that the excess of the ratio $^{21}Ne/^{20}Ne$ relative to that for the terrestrial atmosphere reached 900%.

We have calculated, what mass portion (α) of impurity neon with the given value of the $^{21}Ne/^{20}Ne_{adm}$ ratio should be in a neon separated from meteorite samples for receiving the found inclination of a regression line (b=0.0084). Results are given on Fig. 3. So, for example, at excess of $^{21}Ne/^{20}Ne_{adm}$ value in 9 times in comparison with value of this ratio for an atmosphere (i.e., $K = {}^{21}Ne/^{20}Ne_{adm} / {}^{21}Ne/^{20}Ne_{atm} = 9$), the 23 % of impurity neon in a neon separated from meteorite samples will cause the found value of the coefficient b = 0.0084 (see Table). If the value of K = 5 and, accordingly, $^{21}Ne/^{20}Ne_{adm}$ = 0.0149 then for the found value of b coefficient, a mass portion of impurity neon should be already 45 % (α=0.45; Fig. 3), etc.

There is the essential moment here. We speak on (1) mass portion of impurity neon in a neon separated from the meteorite sample, but not concerning (2) mass portion of contaminant in substance of the meteorite sample. The (2) can be essential less then the (1) at high neon concentration in the contaminant.

Let's return to parameters of the equation of regression lines on Fig. 2 (see Table). For the chromite grains separated from meteorite samples, the value of the a parameter $(0.0081 \pm 0.0013) \times 10^{-8}$ cm^3 g^{-1} at production rate of cosmogenic $^{21}Ne_{cosm}$ of $P_{21} = 7.04 \times 10^{-10}$ cm^3 g^{-1} Myr^{-1} [*Heck et al., 2004; 2008*] corresponds to cosmic-ray exposure age of T_{21} = 0.12 ± 0.02 Myr. This value is apparently the most probable value of exposure age of all found meteorites. The higher values of age calculated by *Heck et al.* [*2004; 2008*] are caused, most possibly, not considered contribution of impurity ^{21}Ne. The value of this contribution increases with reduction of preservation and the sizes of chromite grains. This fact leads to overestimate of exposure ages.

Similar calculation for chromite grains of a terrestrial origin according to the found value of parameter a = $(0.0066 \pm 0.0166)\times10^{-8}$ sm^3 g^{-1} gives value of "exposure age" $T_{21} = 0.09 \pm 0.24$ Myr. This age does not differ from zero within the limits of an error of definition. Let's note, however, rather high error of definition of age in this case, more than on order of magnitude exceeding this for meteorite samples.

Results of the fulfilled analysis allow understanding the reason of overestimate of exposure ages of the fossil meteorites. These results are an additional argument in favour of a hypothesis, that all fossil meteorites found in the south of Sweden can be fragments of one big meteorite which fell out as large shower near the Thorsberg quarry about 470 million years ago approximately in 120 thousand years after catastrophic destruction of the L chondrite parent body.

Table. The parameters of the equation of the regression line $^{21}\mathrm{Ne} = a + b\times{}^{20}\mathrm{Ne}$ for the terrestrial chromite grains (OC) and for grains of fossil meteorites

Samples	a, 10^{-8} cm^3 g^{-1}	b	R
OC (11)	0.0066 ± 0.0166	0.00283 ± 0.00088	0.70 ± 0.16
Meteorites (21)	0.0081 ± 0.0013	0.0084 ± 0.0005	0.78 ± 0.09

Notes: In parentheses, the number of samples is given. R is the correlation coefficient. (According to *Heck et al.* [*2004, 2008*]; *Heck* [2005]; *Meier et al.*[*2010*].)

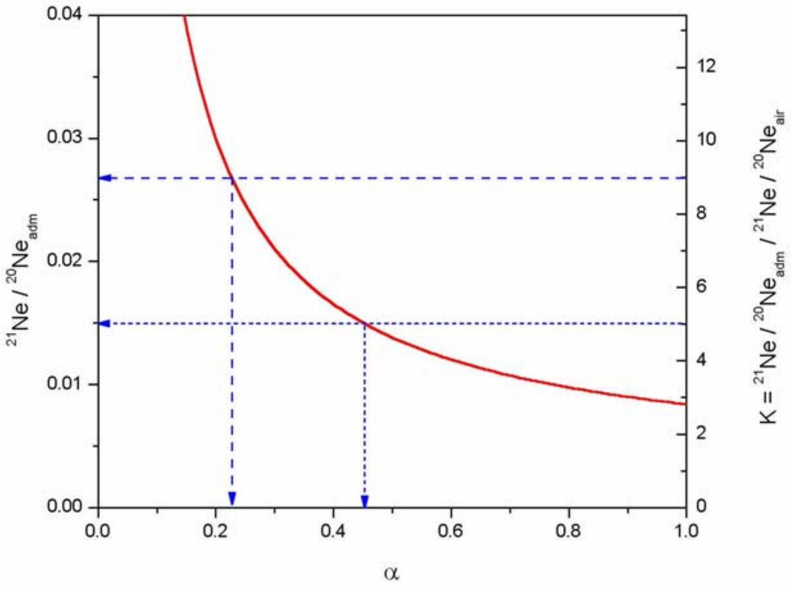

Fig. 3. The interrelation of the $^{21}\mathrm{Ne}/^{20}\mathrm{Ne}_{adm}$ value of impurity neon and the mass fraction (α) of this neon in a neon separated from the meteorite samples for receiving the found value of $^{21}\mathrm{Ne}/^{20}\mathrm{Ne}_{meas}$ =0.0084 (according to Fig. 2 and the Table). The curve equation is $^{21}\mathrm{Ne}/^{20}\mathrm{Ne}_{adm} = (^{21}\mathrm{Ne}/^{20}\mathrm{Ne}_{meas} - {}^{21}\mathrm{Ne}/^{20}\mathrm{Ne}_{atm} \times (1-\alpha))/\alpha$.

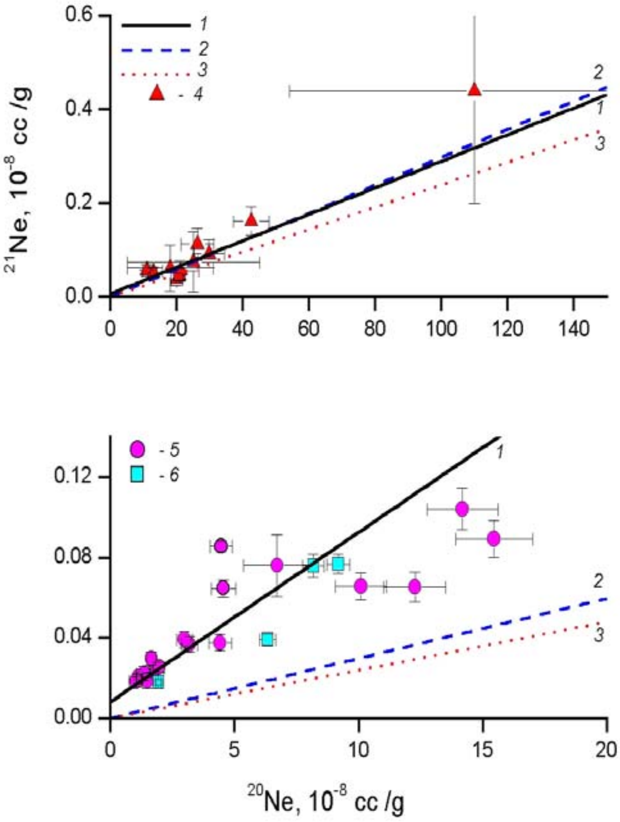

Fig. 2. The ^{21}Ne content vs. ^{20}Ne in the terrestrial chromite grains (*4*; above) and in grains recovered from fossil meteorites (below). *1* – Regression lines; *2* and *3* – interrelations of isotopes of neon of terrestrial atmosphere ($^{21}\mathrm{Ne}/^{20}\mathrm{Ne}$ = 0.00298) and a solar wind ($^{21}\mathrm{Ne}/^{20}\mathrm{Ne}$ = 0.00239), accordingly; *5* – meteorites of non-Ark group; *6* – samples of the Brunflo meteorite. (According to *Heck et al.* [*2004, 2008*]; *Heck* [*2005*]; *Meier et al.* [*2010*].)

This work is supported in part by the Program No. 22 of Fundamental Research of Russian Academy of Sciences.

References:

1. Alexeev, V. A. (2000). Estimating errors in the parameters of the best-fit straight line drawn through data points in geochemical studies, Geokhimiya, No. 8, pp. 909–912 [Geochem. Int. (Engl. Transl.), 2000, vol. 38, No. 8, p. 827].
2. Alexeev, V. A. (2010). Radiation history of fossil meteorites from Sweden, Solar System Research., 44, No. 4, pp. 311-319.
3. Heck, Ph. R. (2005). Helium and neon in presolar silicon carbide grains and in relict chromite grains from fossil meteorites and micrometeorites as tracers of their origin, Diss. ETH No. 16251. Zuricn, 157 p. (http://e-collection.ethbib.ethz.ch/eserv/eth:28217/eth-28217-02.pdf).
4. Heck, Ph. R., B. Schmitz, H. Baur, A. N. Halliday, R. Wieler (2004). Fast delivery of meteorites to Earth after a major asteroid collision, Nature, 430, No. 6997, pp. 323-325.
5. Heck, Ph. R., B. Schmitz, H. Baur, R. Wieler (2008). Noble gases in fossil micrometeorites and meteorites from 470 Myr old sediments from Southern Sweden and new evidence for the L chondrite parent body breakup event, Meteorit. Planet. Sci., 43, pp. 517-528.
6. Meier, M. M. M., B. Schmitz, H. Baur, R. Wieler (2010). Noble gases in individual L chondritic micrometeorites preserved in an Ordovician limestone,

Earth Planet. Sci. Lett. 290, No. 1-2, pp.54-63.

7. Schmitz, B., B. Peucker-Ehrenbrink, M. Lindstrom, M. Tassinari (1997). Accretion rates of meteorites and cosmic dust in the Early Ordovician, Science, 278, No 5335, pp. 88-90.
8. Verkhovskii, A.B., Shukolyukov, Yu.A., and Ashkinadze,G.Sh. (1976). Neon Isotopes in Minerals with Redundant Content of Helium and Argon, Geokhim., No. 3, pp. 315–322.
9. Williamson, J. H. (1968). Least-squares fitting of a straight line, Canadian J. of Physics, 46, pp. 845–1847.

Bagulya[1] A.V., Goncharova[1] L.A., Ivliev[2] A.I., Kalinina[2] G.V., Kashkarov[2] L.L., Konovalova[1] N.S., Okateva[1] N.M., Polukhina[1] N.G., Roussetski A.S., Starkov[1] N. I. Fragmentation of the uranium nuclei in iron-nickel pallasite medium: theoretical estimation of the fragment nuclei superposition with the primary galactic cosmic ray nuclus abundance

[1] Lebedev Physical Institute, RAS, Moscow

[2]V. I. Vernadsky Institute of Geochemistry and Analytical Chemistry, RAS, Moscow bagulya@sci.lebedev.ru; leokash@mail.ru

The simulation results of high energy (400 and 1000 MeV/nucleon) uranium nuclei fragmentation in their interactions with iron and nickel nuclei from pallasite matrix are presented.

Key words: olivine, galactic cosmic ray,charge particle tracks, uranium nuclei fragmentation, iron nickel target

Citaion: Bagulya, A. V., L. A. Goncharova, A. I. Ivliev, G. V. Kalinina, L. L. Kashkarov, N. S. Konovalova, N. M. Okateva, N. G. Polukhina, A. S. Roussetski, N. I. Starkov (2012), Fragmentation of the uranium nuclei in iron-nickel pallasite medium: theoretical estimation of the fragment nuclei superposition with the primary galactic cosmic ray nuclus abundance. *Вестник ОНЗ РАН, 4*,

Introduction. Track analysis of Galaxy cosmic ray (GCR) nuclear component charge spectrum has been carried out by LPI Elementary Particle Laboratory and GEOKHI Cosmology Laboratory since 2006 in the frame of OLIMPIA project [*Ginzburg et al., 2005*]. Olivine crystals extracted from iron-nickel pallacite matrix were used as experimental material.

Method of the nucleus charge identification is based on empirical dependence of the longitudinal track etching velocity from the track residual path [*Kashkarov et al., 2008*]. But due to fragmentation of GCR nuclei, mainly superheavy ones, in pallacite (Fe, Ni)-matrix the number of GCR nuclei registered in olivine is underestimated, while the flux of the secondary light fragments increases.

In the publication the simulation results of high energy (400 and 1000 MeV/nucleon) uranium nuclei fragmentation in their interactions with iron and nickel nuclei from pallacite matrix are presented.

Calculation methods. Numerical calculations of the yield of different fragment nuclei from uranium fragmentation in uranium-iron and uranium-nickel interactions were held with a help of Monte-Carlo simulations on base of GEANT4 program [*Agostinelli et al., 2003*]. GEANT4 energy loss algorithm takes into account all possible mechanisms of ion passing through the matter. In particular, the stopping power values are determined with Bethe-Bloch relation and the data are extrapolated numerically on base of ICRU (International Commission on Radiological Units and Measurements) tables.

In the calculations there was used the Hadr01 program, an official component of GEANT4 which was worked out with participation of LPI colleagues. The program allows to simulate different nucleus beams passing through the matter. The results are presented as different distributions of primary and secondary nuclei available for analysis. The most informative parameters are those which characterize the energy loss of primary beam nuclei along their stopping tracks, and besides, the secondary particle energy and charge values. Test calculations of different energy ^{131}Xe, ^{207}Pb and ^{238}U nuclei passing through the various materials are already held. The results show good agreement in error limits with table data [*Hubert et al., 1990*] containing the stopping power and path values for ions with 2≤ Z≤ 103 in the energy region from 2.5 to 500 MeV/nucleon for different materials.

Results and discussions. The following plots and tables present the numerical results of the yield of fragments from uranium interactions with $Fe_{0.9}$ and $Ni_{0.1}$ target nuclei.

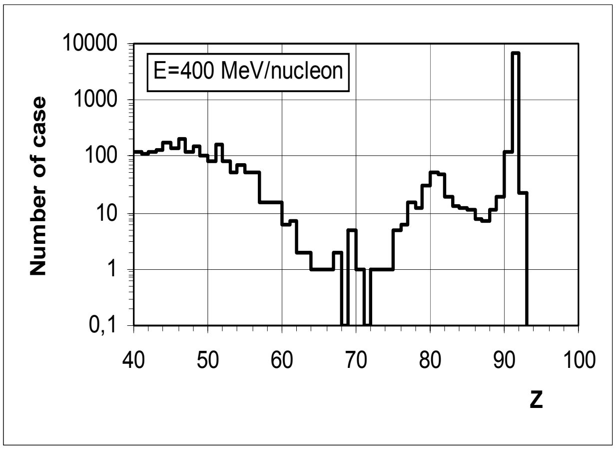

Fig. 1. Nuclear composition of fragments from accelerated uranium nuclei (E = 400 MeV/nucleon) interactions with $Fe_{0.9}$ $Ni_{0.1}$ 10 mm target

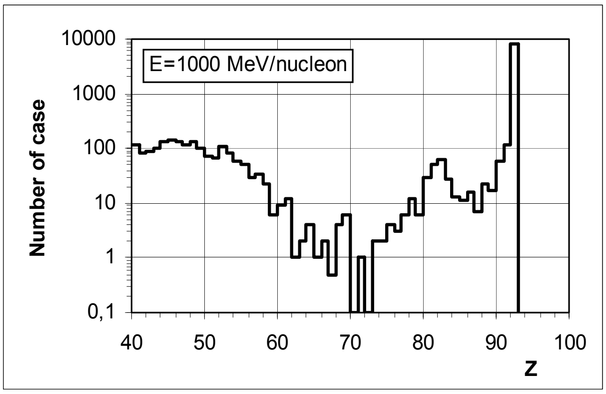

Fig. 2. Nulear composition of fragments from accelerated uranium nuclei (E = 1000 MeV/nucleon) interactions with $Fe_{0.9}Ni_{0.1}$ 10 mm target.

Fragmentation of uranium nuclei with E_o = 95 GeV. Depending on the energy the fragment nuclei range in the olivine crystals, contacted with Fe $_{0.9}$Ni $_{0.1}$-matrix, can be equal from tenths up to some millimeters due to energy from ~ 10 MeV/nucleon up to ~ 1000 MeV/nucleon, correspondingly.

Energy and residual range (RR_{ol}) distributions for the particles in olivine crystals of pallasite $Fe_{0.9}Ni_{0.1}$- matrix are presented in Table 1.

Special attention was paid to the II and III groups of nuclei with RR_{ol} values in interval from ~ 1.0 to ~ 0.15 mm, corresponding to "cylindrical" zone of the etched part of track. Flux of these nuclei makes ~ 50% of $N_{U,o}$. Making ~7% of $N_{U,o}$ the I group nuclei get into olivine and form tracks in their "needle" extended zone. The IV group nuclei make rather short path track background ($RR_{ol} \leq 0.15$ mm) with a density ~ 40% of $N_{U,o}$.

Fragmentation of uranium nuclei with E_o = 238 GeV. The energy distribution of the uranium nuclei behind the target (10 mm of $Fe_{0.9}Ni_{0.1}$ - matrix) shows a peak at E = (180 ± 10) GeV formed by ~1100 nuclei, what makes 10% of $N_{U,o}$. The peak is formed by the initial beam uranium nuclei which have lost ~60 Gev from their energy after passing the target. Their RR_{ol} is about 25 mm. The number of uranium nuclei with RR_{ol}=0.5-1.0 mm (at E_U = 20 ± 2 GeV) equals 520 (~ 0.5% of $N_{U,o}$). Uranium nuclei with RR_{ol} from ~ 1 to ~ 20 mm, which tracks are formed in the "needle" zone, make the major (~ 90%) group of nuclei.

Table 1. Energy and residual range (RR_{ol}) distributions for the uranium nuclei in olivine crystals 10 mm from $Fe_{0.9}Ni_{0.1}$-target

Nuclear group	E, GeV	RR_{ol}, мм	ΣN_U	$\Sigma N_U/N_{U,o}$ $^{(*)}$
I	30.5–22.5	1.7–1.0	683	~ 0.07
II	22.5–13.5	1.0–0.5	2124	~ 0.2
III	13.5–5.0	0.5–0.15	3108	~ 0.3
IV	≤ 5.0	≤ 0.15	4085	~ 0.4

$^{(*)}$ Initial beam contents $N_{U,o}$ = 10000 uranium nuclei.

Table 2. Relative yield of the fragment nuclei from interactions of uranium nuclei with E_o = 95 GeV and 10 mm $Fe_{0.9}Ni_{0.1}$ - target

Nuclear group		ΣN_Z $^{(*)}$	$\Sigma N_Z/N_{U,o}$
№	Z		
I	40–49	1253	0.13
II	50–59	585	0.059
III	60–69	27	0.0023
IV	70–79	72	0.007
V	80–89	192	0.019
VI	90–92	7142	0.71

$^{(*)}$ Initial beam contents $N_{U,o}$ = 10000 uranium nuclei.

The fragment nuclei yield. In Table 2 there are presented the numerical results of the yield for different nuclei conventionally separated in six groups. The data were prepared for the initial uranium beam energy E_0=95 GeV.

Total yield of fragment nuclei with Z≥40 makes about 50% of $N_{U,o}$. About 7% of this number are formed by II, III and IV groups. Fragment nuclei with Z in the interval 80–89 are observed about 20%. Maximum contribution about 70% is made by nuclei with Z in the interval 90–92.

Results for primary uranium beam with E_0=238 GeV are presented in Table 3.

Table 3. Relative yield of the fragment nuclei from interactions of uranium nuclei with E_o = 238 GeV and 10 mm $Fe_{0.9}Ni_{0.1}$ - target

Nuclear group		ΣN_Z $^{(*)}$	$\Sigma N_Z/N_{U,o}$
№	Z		
I	40–49	1145	~ 0.11
II	50–59	529	~ 0.053
III	60–69	35	~ 0.0035
IV	70–79	36	~ 0.0036
V	80–89	258	~ 0.026
VI	90–92	8180	~ 0.82

$^{(*)}$ Initial beam contents $N_{U,o}$ = 10000 uranium nuclei.

In the fragment-nuclei charge distribution, across of 8180 slowed-down uranium nuclei (~ 82% of initial uranium flux $N_{U,o}$), superhigh nuclei fraction (Z = 80–89) exclusive of 258 that is near of 2.5%. The fragment-nuclei with charge in interval 60–79 consist only ~ 0.7%. Approximately of 10% and 5% fall on the nuclei of I-st and II-nd groups, accordingly.

Conclusions. Numerical estimation of fragment nuclei yield after uranium interactions in 10 mm $Fe_{0.9}Ni_{0.1}$ – target shows:

Output of secondary nuclei with charge in intervals of 40 < Z < 49 and 50 < Z < 59 make up ~ (11–13) % и ~ (5-6) %, relatively to initial uranium flux.

Nuclei with charge in intervals of 60 < Z < 79 make up smaller of ~ 1% from the total number of formed fragment-nuclei.

About (2-2.5)% of fragment nuclei yield with Z = 80–89.

Part of the actinide group (Th-U) nucleus with Z = 90-92 and energy 400-1000 MeV·nucleon^{-1} do not underwent to fragmentation process in $Fe_{0.9}Ni_{0.1}$ – target of 10 mm thickness make up ~ (70–80)%.

Preliminary estimation of superposition of the fragment nuclei over GCR nucleus flux in the region 50<Z<89 gives not higher ~ 10 percents which are to be taken into account in track experiments on GCR charge composition.

The work is supported by RFBR grant №10-02-00375-a and in part by the Program No. 22 of Fundamental Research of Russian Academy of Sciences.

References:

1. Agostinelli, S., et al. (2003). GEANT4 Collaboration, *Nucl. Instr.& Meth.,* vol. A506, p. 250.
2. Ginzburg, V. L., N. G. Polukhina, E. L. Feinberg, et al. (2005). Problems and Horizons of the Search for Tracks of Heavy and Superheavy Nuclei in Olivine Crystals from Meteorites (OLIMPIYA project), *Doclady Physics*, vol. 50, p. 283–285.
3. Hubert, F., R. Bimbot, H. Gauvin (1990). *Atomic Data and Nuclear Data Tables* 46, p. 1.
4. Kashkarov, L. L., N. G. Polukhina, N. I. Starkov, et al. (2008). Geometrical track parameters in the pallasite olivine: Identification of the cosmic ray heavy nuclei, *Radiation Measurements*, vol. 43, p. S266–S268.

Barenbaum A.A. On the asymmetry of the surface terrestrial planets, caused by the falls of galactic comets

Institute of Oil and Gas Problems RAS, Moscow azary@mail.ru

We present the hypothesis according to which a similar asymmetry the surface of terrestrial planets, which consists in the predominance of the "continents" in the southern hemisphere and "seas" in the northern hemisphere is caused by the bombardment by galactic comets during the period of 5÷1 Ma. Fallings of galactic comets on the planets without an atmosphere create large craters, and on the planets with the gas shall were lead to significant uplifts of the surface that exposed to cometary bombardment.

Key words: [galactic comets, craters, planets, newest uplifts of continents]

Citaion: Barenbaum (2012), On the asymmetry of the surface terrestrial planets, caused by the falls of galactic comets, hydrocarbons, *Vestn. Otd. nauk Zemle, 4*

Introduction. A number of large celestial bodies in the solar system, in particular, Mars and the Moon have a similar asymmetry of the surface. Their sublime "continental" areas of surface are predominate in the southern hemisphere, whereas their "marine" areas are located in the north hemisphere. Our Earth also has the "oceanic" hemisphere and the "continental" hemisphere. This asymmetry explained by different reasons. For the Earth and the Moon this reason is the separation of the Moon from the Earth [*Darvin, 1910*], or a blow on the Earth of the cosmic body of planetary size [*Hartman, Davis, 1975*]. The appearance of asymmetry of Mars also explained by powerful impact event [*Wikipedia*].

Currently, the main relief-forming factor is considered to be fallings on a planet of large cosmic bodies. There are planetesimals that can to form the planets on early stage of their education, as well as asteroids and comets existing in the interplanetary space now. But interplanetary asteroids and ordinary comets – that is not all cosmic bodies that was falling to the planets in the Phanerozoic. The comets which born in the Galaxy were falling to all planets in the much larger number. These comets are generated into zones condensation of gas of the galactic arms and they are enter to the Solar system at the time of finding the Sun in jet streams and the spiral arms of the Galaxy.

The comets from closest to Sun jet stream Orion-Cygnus, falled on planets during period 5÷1 Ma are the best studied. Their speed relative to the Sun is 450 km/s, their mass $\sim 10^{12} \div 10^{17}$ g, and kinetic energy is $\sim 10^{20} \div 10^{25}$ J. The density of the comets nuclei is ~1 g/cm^3. On 80–90% galactic comets are composed of water ice, and 10–15% of the carbon component [*Barenbaum, 2010*].

Objectives of the article. Many facts [*Barenbaum, 2002, 2004, 2008; Barenbaum, Shpekin, 2011, etc.*] give the evidence to suggest that similar asymmetry surface of different planets, consisting in predominance "continents" in the southern hemisphere and "seas" in the northern hemisphere, was generated on the planets due to falls comets of jet stream Orion-Cygnus in the period 5-1 million years ago. It was then on the Earth took place a rapid uplifting continents [*Artyushkov, 2008*], and on Mars, Moon and Mercury, along with this process originated craters [*Barenbaum, 2002*].

The rationale of this hypothesis, proposed below, based on the following basic information about the galactic comets and their interactions with the terrestrial planets [*Barenbaum, 2010*]:

The number galactic comets were falled on the planet throughout the Phanerozoic in the hundreds or thousands times greater than the interplanetary asteroids and comets of the same dimensions. On planets without an atmosphere, these comets are generate craters ≥10 km in diameter, which are very different in many respects from the craters which produced asteroids and comets.

In contrast to the interplanetary asteroids and comets falling on the planets randomly, the galactic comets are falling in form "cometary rain". Duration of one cometary rain is ~2÷5 million years, and they cycled repeated through 19-37 million years. Depending on the situation in the Galaxy, the number comets in the showers varies from one to two orders of magnitude. During one bombardment on the Earth may fall $10^4 \div 10^6$ comets. The latest cometary rain took place 5÷1 Ma and has been a relatively "weak." According to our estimates for this time on the surface of planets with area 100×100 km^2 could fall 3–5 galactic comets.

Such density fallings of galactic comets, however, is sufficient to completely saturate the surface by craters with diameter 10÷200 km. Limit saturated by these craters the surfaces of the Moon, Mercury and Mars theoretically is about ~100 craters in the area of 1 million km^2. Calculations show that in saturation state funnels of craters occupy 50% all surface.

An important factor causing the anisotropy of planets surface, is the obliquity of the plane ecliptic at an angle of 62° to the plane of the Galaxy in which the comets moved. The available evidence suggests that the last time the galactic comets mainly fell on the southern hemisphere planets, the axis rotation of which is perpendicular to the ecliptic or deviates from this direction weakly. Among them the Earth, Mars, and Mercury, as well as the Moon.

The presence gaseous envelope at planet radically changes the physics of the interaction galactic comets with the planets. In the atmosphere of the Earth galactic comets are completely destroyed, forming hypersonic jet consisting of evaporated cometary material and shock heated air. Reaching the surface, this jet does not create a crater and uses the most part its energy to heat ~100-200 km layer of rocks under the place of comet impact. In the future this thermal energy is released in different tectonomagmatic processes. In the oceans and seas this are, above all, the outpouring of lava to the bottom and the formation seamounts, and on the continents are the uplifting surface and the formation intrusions [*Barenbaum, 2008, 2011*].

In the atmosphere of Mars, to 100 times less dense than at the Earth, the nuclei of galactic comets partially evaporate, which leads simultaneously to two effects: to lifting continental surface and to appearance of craters on it. At this, however, craters on Mars turn out systematically smaller in diameter than for example on the Moon and Mercury, which have not the gas shells.

We illustrate this conclusions using relevant evidence.

Factual data and its discussion. In Fig. 1a shows a relief map of Mars, and in Fig. 1b shows the area occupied by funnels craters on both sides of the border in Fig. 1a.

In Fig. 1a schematically shown surface of the Mars, which is segregated the tectonic boundary into two hemispheres: the southeastern of tectonically passive – "continental" and the northwestern tectonically active – "maritime". Continental hemisphere is known to be elevated above the maritime by 2–6 km, and completely covered with large craters, whereas surface of the maritime hemisphere is presented of smooth plain with few amount of craters. The boundary between the hemispheres also is unusual. She is obtained as the trace of the cross section of a spherical surface of Mars by the plane inclined to his rotation axis at an angle of 35° [*Kazimirov, 1977*].

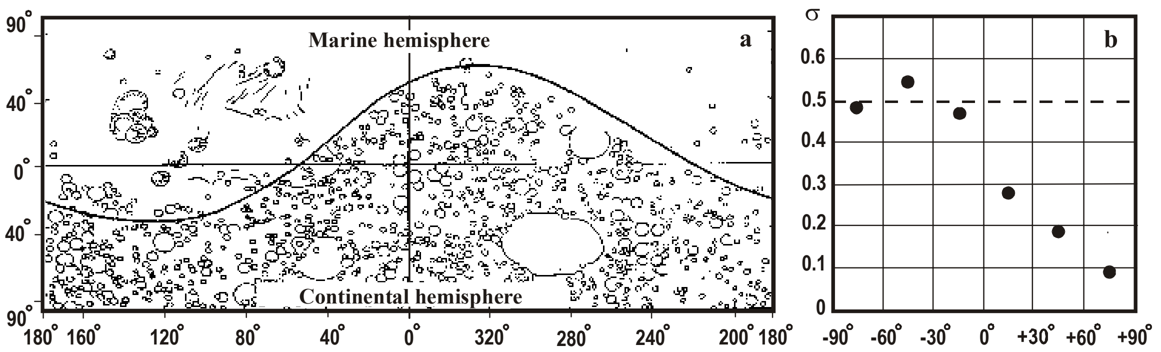

Fig. 1. a) The asymmetric structure of the surface of Mars [*Shaded relief map of Mars, 1972*]. Line shows the boundary between the "maritime" and the "continental" hemispheres of Mars, separating the regions with different density of large craters [*Kazimirov, 1977*]; b) Calculation of the share surface of Mars under craters with a diameter ≥ 10 km in the bands of latitude 30° on both sides of the border [*Barenbaum, 2002*], dashed line – the theoretical limit saturation of the surface by craters with diameter ≥ 10 km

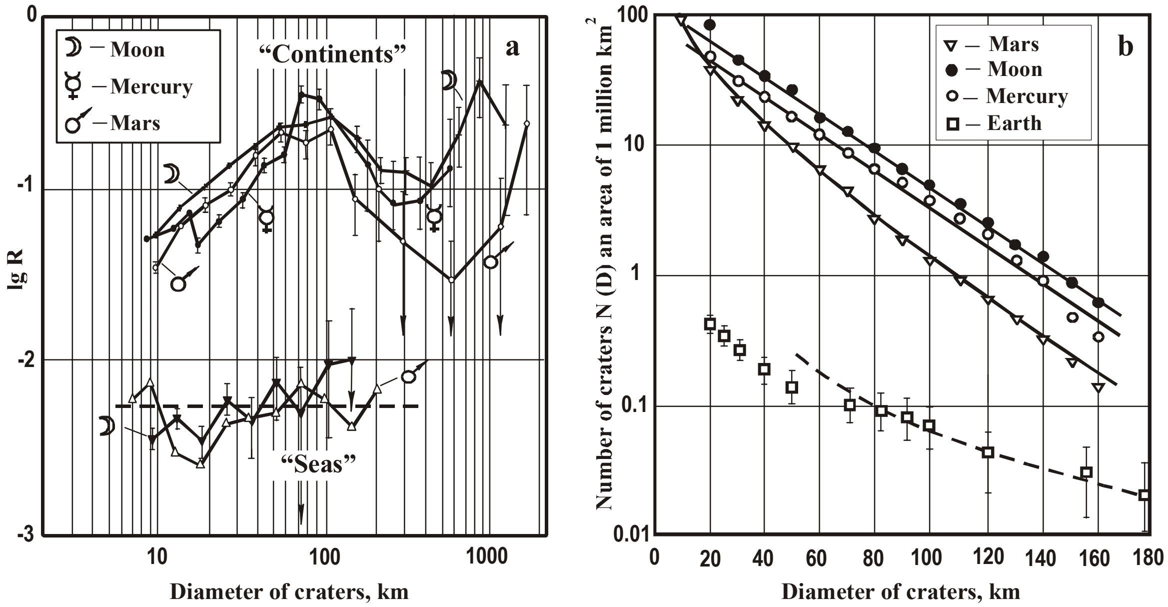

Fig. 2. The distributions of the density craters by diameter: a) the differential dependence $N(\Delta D)$ with step $\Delta D = D \div \sqrt{2}D$ in a special log-scale [*Voronow et al, 1986*] and b) the integral dependence $N(> D)$ in a semi-logarithmic scale [*Barenbaum, 2002*], constructed according to data [*Kazimirov et al, 1980*]. The dashed line on both pictures corresponds to the back quadratic dependence by D

In Fig. 1b shown calculated according to data [*Kazimirov et al, 1980*] portion of the surface Mars covered by craters on both sides of his tectonic boundary. From the calculations follows that the continental hemisphere of Mars is maximal saturated by craters. Moreover if in this hemisphere cometary craters are dominated, on the equator of the Mars amount craters created by comets and asteroids becomes equal, and at the North pole Mars the cometary craters practically disappear.

Topographic features of the Mars we associate with falling galactic comets to its southeastern hemisphere perpendicular to the plane of the tectonic boundary. The difference in height between the hemispheres, according to our estimates [*Barenbaum, 2004*], can be explained by heating to the status of partial melting the layer rocks of lithosphere under continents by the thickness 100–250 km. The presence in the equatorial region of maritime hemisphere of four volcanoes in height from 15 to 25 km also indicates the existence martian asthenosphere.

Distributions of craters on the Mars, the Moon, the Mercury, as well as on the Earth are shown in Fig. 2. We see (Fig. 2a) that the craters on the continents are not only considerably exceeding amount craters on the seas, but they also differ in the distribution of diameters. If the craters on the seas obey to the back quadratic dependence, the craters on the continents are distributed exponentially (Fig. 2b), by analogy with the galactic comets. In comparison with the Moon and the Mercury, the martian continents depleted by large cometary craters. On Earth cometary craters are absent altogether. All Earth's craters formed by asteroids, and their deviation from the distribution by the back quadratic dependence is caused by observational selection.

In the process of orbital Sun motion in the Galaxy, the galactic comets bombard the different areas of the planet, in result zone of maximal fall comets moves along the spherical surface of planets. In Fig. 3 the density of falling galactic comets to the Earth, calculated for the last 700 Ma [Barenbaum, 2002], we compare with the borders cycles Bertrand by data [*Khain, 2000*], with the periods existence of the supercontinents Pangea and Pannotia by data [*Bozhko, 2003*] and with the latitude distribution of glacial covers by data [*Chumakov, 2001*].

By comparing the calculation results with actual data it should be borne in mind that the flux of galactic comets bombarding the Earth greatly variety. The number falling comets significantly depend on the position of the Sun in an orbit, and sharply increase in the zones gas-condensation in the galactic arms. The comets most intense were falling in the late Cambrian and Ordovician and the Triassic. In order to simplify the analysis results of the calculation, this circumstance in Fig. 3a is not reflected. In the calculations we also ignored the precession and nutation of the Earth's axis and assumed that the ecliptic plane has a precession with period 2.7 billion years in the direction coinciding with motion of the Sun in the Galaxy.

According to Fig. 3a the galactic comets are alternately bombard the northern and the southern hemispheres of the Earth. Moreover, due to changes the orbital velocity of the Sun, the comets fall on the southern hemisphere longer time than on the northern. Thereby the surface in southern hemisphere ascends more active. By this circumstance we explain [*Barenbaum et al, 2004*] the processes of agglomeration supercontinents in the southern hemisphere as well as the latitudes of the spread ice sheets (Fig. 3c) which arisen on the places of cometary fallings.

It should be noted the surface of Earth’s southern hemisphere rises today. According to the GPS data the average radius of southern hemisphere is growing annually by about 1.37 mm, whereas radius of the northern hemisphere shows no growth [*Barkin, 2007*].

The calculations of the density fallings comets in the period of the last bombardment in full can be applied to the Mars, the rotation axis of which is tilted like the Earth.

Phenomenon of newest uplifts. This name has been given to the phenomenon simultaneous surface uplift of almost all the continents of the Earth, which took place during the period from 5 to 1 million years ago. Height of the raises was greatly varied. On the Pacific coast, height of the raises had reached the first few hundred meters, on the Siberian platform – 200–1000 m, in South Africa – from 300-400 m in the west and up 900–1200 m of the east. The fastest growth occurred in the mountainous terrain. For example, the Arabian platform increased its height by 2 km, the Alps – by 3 km, and the Himalayas – by 6 km. Under most of the mountains there was a significant rise of the asthenosphere that in some places led to an outpouring of magma to the surface.

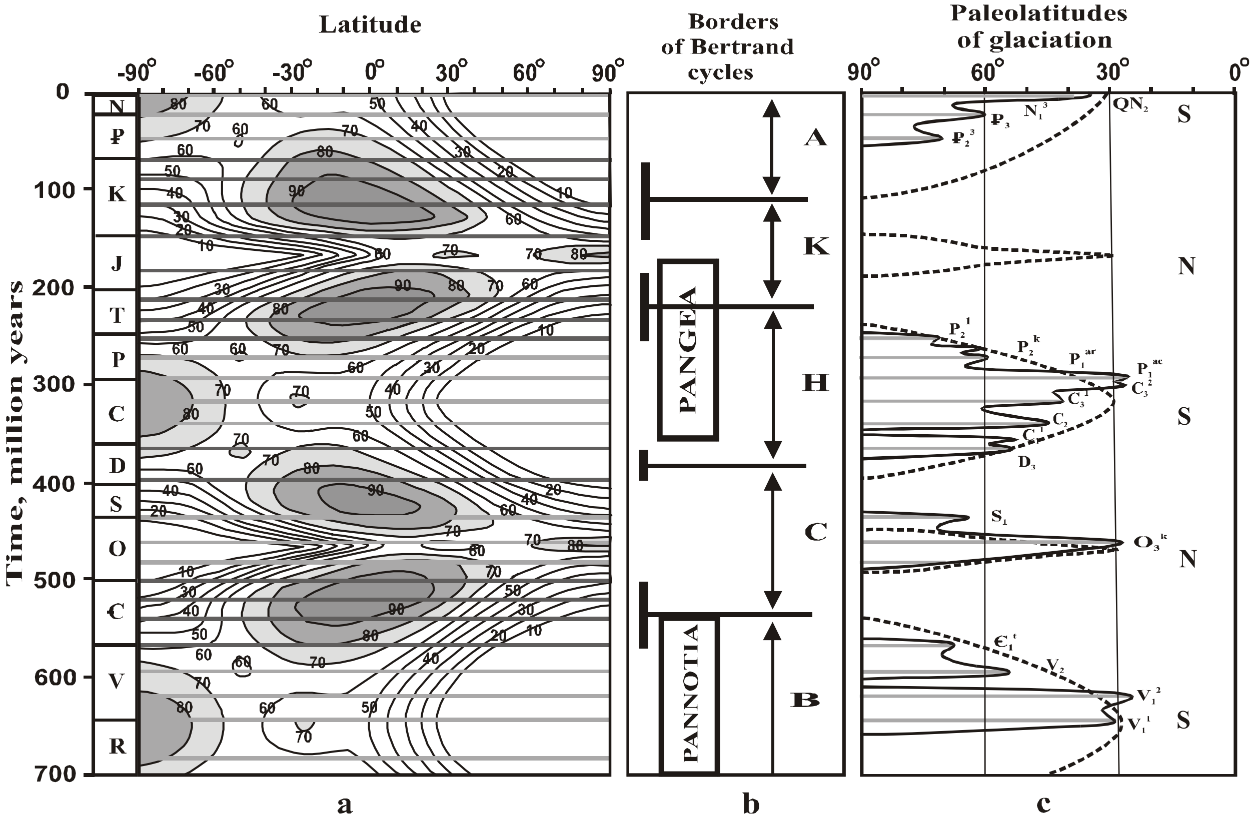

Fig. 3. Comparison of the density fallings galactic comets to Earth (a) with the borders of cycles Bertrand [*Khain, 2000*] and with periods of existence supercontinents Pangea and Pannotia [*Bozhko, 2003*] (b), and as well as with the paleolatitudes propagation ice covers [*Chumakov, 2001*] (c). Narrow horizontal bars show the times of cometary bombardment, taken 5 million years. Shown darker color the cometary bombardment, corresponding to the borders cycles Bertrand: C – Baikal, C – Caledonian, H – Hercynian, K – Cimmerian and A – Alpine. The calculations outside the horizontal bars have no meaning. The figures have lines of isodences indicate percentage of maximum intensity, accepted equal 100%. At Fig. c the dotted line indicates the angle between the direction of the Galactic center and the Earth's axis, which defines the region paleolatitudes fallings comets. N and S – the "northern" and "southern" glaciations.

The Phenomenon of newest uplifts is explained [*Artyushkov, 2008*] by replacement a layer of the continental lithosphere thickness of ~100 km on layer of hot asthenosphere. As a result the viscosity in the replaceable layer is reduces by 4 orders of magnitude, and the temperature is an increase by hundreds of degrees Celsius. Our estimates show [*Barenbaum, 2008*] that for the explanation of the newest uplifts is needed energy $\geq 10^{27}$ J.

We [*Barenbaum, 2012*] evaluated the thermal effect that is created by falling on the Earth galactic comets of various energies. The calculations were performed for a cube of rocks with sides 100 km under the assumption that the comet's energy expended on heating of rocks, is distributed in the volume of a cube evenly. We calculated heating temperature and the corresponding to this temperature the elongation edges of a cube. It is shown that by heating of the column rocks by length 100 km for every 100°, it elevates Earth's surface by 300 m. But if for small comets these effects are small the comet with the energy of $\sim 10^{25}$ J heats the substance more than 1000° that leads to a complete melting of the rocks in the volume 10^6 km^3.

Comets such energies, however, is very small. At the time of last bombardment their probability falling to area 100×100 km^2 is order of $\sim 10^{-3}$. For comets medium-energy $\sim 10^{22}$–10^{24} J likelihood of falls on the same area are much higher. Such comets heat the rocks at hundreds of degrees, and they are able to provide lift of Earth's surface for miles.

These estimates are well consistent with the observed height of newest uplifts as well as with the degree of heating of underlying rocks. Clearly, that fallings of galactic comets can to produce highly non-uniform heating the rocks of the lithosphere beneath the continents in the lateral plane, and as in depth. Undoubtedly and the fact that additional heating of rocks at the lower boundary of the lithosphere in a state close to the liquids, inevitably leads to the melting and to chemical transformation of minerals in the processes of eclogitization.

Thus we can assert the fallings of galactic comets leads to origin at the base of the lithosphere the thick layer of rocks, which may be nonuniformly heated and partially molten. This layer we can justifiably be named as the asthenosphere. The existence of the asthenosphere it is characteristic phenomenon not only for the Earth but as well as for all terrestrial planets. The appearance of this layer under the Earth's continents leads to a significant raise of their surface, and under the oceans bottom leads to the intense outpouring of lava, especially in the zones of mid-ocean ridges.

Summary and conclusions

1. The modern predominance of sublime "continental" regions of the surface planets in the southern hemisphere and of low "marine" regions in the northern hemisphere, it is mainly consequence the bombardment of the planets by the galactic comets in period 5÷1 Ma.

2. Fall galactic comets are a general cause of the raise considerable parts of the planet surface and appearance of large impact craters on the same surface. The surface rises on planets with dense atmosphere, whereas the craters arise on the planets without the atmosphere. On the Mars, which possesses a rarefied gas environment this two processes occur simultaneously.

References:

1. Artyushkov, E. V. (2008). Newest uplifts of crystal on the continents as a consequence of rapid softening of the lithosphere mantle and of its replacement by asthenosphere, *General and regional problems of tectonics and geodynamics*, v.1. Moscow: GEOS, p. 31–34 (in Russian).
2. Barenbaum, A. A. (2002). *Galaxy, Solar system, Earth. Subordinated processes and evolution*, Moscow: GEOS, 393 p (in Russian).
3. Barenbaum, A. A. (2004). On a one particularity of asthenosphere of the Mars, *Vestnik Otdelenia nauk o Zemle RAN*, №1 (22)'2004 URL: http://www.scgis.ru/russian/cp1251/h_dgggms/1-2004/informbul-1/planet-14.pdf
4. Barenbaum, A. A. (2008). Processes in the Earth crust and upper mantle: problems of the mountain building and the newest terrestrial crust elevation, *Connection between surface structures of the terrestrial crust with deep-seated ones*, Materials XIV Intern. Conference. Petrozavodsk, Karelian Science Center RAS, P.1, p. 43-47 (in Russian).
5. Barenbaum, A. A. (2010). *Galaxycentric paradigm in geology and astronomy*, Moscow: PH LIBROKOM, 544 p (in Russian).
6. Barenbaum, A. A. (2011). Tectonomagmatic processes in the oceans and on the continents as the indicators fallings of galactic comets. Internal, Conference dedicated memory V. E. Khain: *The modern state of the Earth sciences*, Moscow: MGU. http://khain 2011.web.ru. p. 166–171 (in Russian).
7. Barenbaum, A. A. (2012) On the origin of newest uplifts of the Earth crust: a new formulation of the problems of global geodynamics (in press).
8. Barenbaum, A. A., V. E. Hain, N. A. Yasamanov (2004). Large-scale tectonic cycle: an analysis from the standpoint of the galactic concept, *Vestnik MGU, Ser.4, Geology,* №3, p. 3–16.
9. Barenbaum, A. A., M. I. Shpekin (2011). On the age of the lunar surface, *Vestnik Otdelenia nauk o Zemle RAN*, v.3, NZ6011, doi:10.2205/2011NZ000141.
10. Barkin, Yu. V. (2007). Mechanism of increase in mean sea level and the decision of "attribution problem", *Geology of the seas and oceans*, v. IV, Moscow: GEOS, p. 21–23 (in Russian).
11. Bozhko, N. A. (2003). Super-continental cyclicity in the tectonic development of the lithosphere, *Tectonics and geodynamics of the continental lithosphere*, v.1, Moscow: GEOS, p. 56–60 (in Russian).
12. Chumakov, N. M. (2001). Periodicity of main glacial events and their correlation with the endogenous activity of the Earth, *Doklady Akad. Nauk*, v. 378, №5, p. 656–659 (in Russian).
13. Darvin, G. H. (1910) *Scientific Papers*. *V.III.* Cambrige.
14. Hartman, W. K., Davis, D. R. (1975) Satellite-sized planetesimals and lunar origin. *Icarus. V.24*. p. 504–515.
15. Kazimirov, D. A. (1977). De-symmetry of terrestrial planets and satellites and the main phase of their development. *Questions of planetary tectonogenesis*. *Pr. GIN. Issue 1*. Moscow. p. 23–66 (in Russian).
16. Kazimirov, D. A., B. D. Sitnikov, G. A. Poroshkova and others (1980). *Density distribution of craters on the Moon, Mercury and Mars.* Preprint GIN-GAISH (in Russian).
17. Khain, V. E. (2000). Large-scale cyclicity in the tectonic history of the Earth and its possible causes. *Geotektonika.* №6. p. 3–14 (in Russian).
18. *Shaded relief map of Mars* (1972). 1:25000000.
19. Voronov A., R. G. Strom, M. Garkis (1986). Interpretation of crater chronicles: from Mercury to Ganymede and Callisto. *Satellites of Jupiter*. *Part 2*. Moscow: Mir, p. 5–48 (in Russian).
20. *Wikipedia*. http://ru.wikipedia.org/wiki/Mars (planet)

Buikin [1]A.I., Verchovsky [2]A.B., Lorentz [1]K.A., Skripnik [1]A. Ya. Study of isotopic and elemental compositions of gases from Pesyanoe by stepwise crushing

[1]V. I. Vernadsky Institute of Geochemistry and Analytical Chemistry, RAS, Moscow Bouikine@mail.ru

[2]The Open University, UK

At the first time for meteorites we performed investigation of Ar, N_2, Ne isotope composition and He, Ar, Ne and N_2 elemental ratios in fluid inclusions in pyroxenes of different generations (dark Px-G, containing high amount of fluid inclusions, and light non-transparent Px-B with lower amount of fluid inclusions) from

aubrite Pesyanoe. Both samples contain nitrogen in fluid inclusions with similar isotope composition (-12 to -30 ‰ Atm), but differ in Ar isotope composition: Px-B is characterized by more radiogenic argon ($^{40}Ar/^{36}Ar$ = 110–170), while Px-G contains argon with higher proportion of solar argon and smaller variations in $^{40}Ar/^{36}Ar$ ratios (35–42). The samples as well differ in neon isotope composition – in Px-B it is considerably more cosmogenic. We also have shown that light nitrogen is situated mostly in fluid inclusions, and made an assumption that heavy nitrogen component (with positive $\delta^{15}N$ values) can be primary magmatic in origin.

Key words: Pesyanoe, He, Ne, Ar, N_2, CO_2, fluid inclusions, stepwise crushing

Reference: Buikin, A. I., A. B. Verchovsky, K. A. Lorenz, A. Ya. Skripnik (2012), Study of isotopic and elemental composition of gases from Pesyanoe by stepwise crushing method, *Vestnik ONZ RAS, 4*,

Dorofeeva[1,2] V. A., Vagina[2] O. V. Equations of temperature dependence of ice capacity and some clathrats hydrats formed in H–O–C–N–Ar–Kr–Xe system at low temperatures and pressure

[1] V. I. Vernadsky Institute of Geochemistry and Analytical Chemistry RAS, Moscow

[2] Dubna International University of Nature, Society, and Man, Dubna dorofeeva@geokhi.ru

For the study of phase equilibrium in H–O–C–N–Ar–Kr–Xe system at low temperatures (T<100K) and pressure ($P < 10^{-6}$ bar) we were obtained coefficients of semi-empirical equation of the temperature dependence of heat capacity for ice, CO_2(cr) и NH_4OH(cr) proposed by I.L. Khodakovsky

Key words: [cosmochemistry, modeling, thermodynamics, heat capacity, ice, clathrats hydrats]

Reference: Dorofeeva, V. A., O. V. Vagina (2012), Equation of temperature dependence of ice capacity and some clathrats hydrats formed in H—O—C—N—Ar—Kr—Xe system at low temperatures and pressure, *Vestnik ONZ RAS, 4, (doi:)*

One of the most important problems of modern cosmochemistry is genesis of volatiles in Titan and Enceladus which are regular satellites of Saturn. During the space mission «Cassini» it was found that the main components of the atmosphere Titan are nitrogen and methane and there are in significant quantities NH_3, N_2, CH_4, CO и CO_2 in the plume of Enceladus. Heretofore, their origin isn' t known – whether it was the primary gases of the solar protoplanetary disk (nebula), accumulated by ice planetesimals, which were formed in the area of Saturn, some of them have already been formed in the bowels of the satellites in the action of their evolution. Model reconstruction of the accumulation of volatiles from the nebula gas phase requires thermodynamic information for all components potentially possible in H–O–C–N–Ar–Kr–Xe system, including condensed phases, crystalline and clathrate hydrates formed in the solar system composition at low temperatures (T <100K) and pressures ($P < 10^{-6}$ bar).

However thermodynamic information for a number of condensed and solid phases as well as clathrates hydrates in these PT conditions is not full enough. This is due to the fact that in the Earth's formation of such phases is associated with much higher pressures and temperatures than in a nebula, for example, the formation of methane clathrate hydrate methane in the deep sea.

Moreover all the necessary experimental information is fragmentary and often not easily accessible. Unfortunately nowadays there are not reference books providing us with the results of experimental measurements and recommended values of thermodynamic and thermoelastic properties of substances for the temperature range from 0 to 273 K.

It is necessary to have the equation of heat to get functional dependencies of the thermodynamic properties of these components on temperature: $C_P = C_P(T)$.

Table 1 presents the results of experimental data search based on heat capacity measurements for some substances as well as the temperatures in which the measure passed.

The semi-empirical equation of the temperature dependence of heat capacity $C_P(T)$ proposed by I.L. Khodakovsky was used as an analytical function.

$$C_P = Rn[\boldsymbol{k}L_D + (3 - \boldsymbol{k})L_E)] + \alpha_T^2 V_T K_T T \qquad (1),$$

where $L_D = [1 - 1/(1 + bT^3)]$, $L_E = [1 - 1/(1 + cT^2)]$,
R – gas constant, n - the number of atoms in a molecule,
α_T – volume coefficient of thermal expansion,
K_T – isothermal bulk modulus,
V_T – volume of one gram mole of a substance,
T – temperature,
B, c and $\boldsymbol{k}$, – empirical coefficients.

Table 1. Experimental data of measurements of a thermal capacity for substances under consideration

System	T (K) for C_p	Reference
Kr Xe	0.4–12	[*Finegold et. al, u дp, 1969*]
H_2O(cr)	0.5–38 40–273.15	[*Smith et al, 2007*] [*Giauque et al,1936*] [*Glushko et al, 1978*]
CO(cr)	0.8–4.2	[*Burford et al,1969*]
CO_2(cr)	2–20 15–195	[*Manzhelii et al,1971*] [*Giauque et al, 1937*]
CH_4(cr)	0.4–28	[*Vogt et al, 1976*]
Kr·5.66H_2O(cr)	7–115 85–270	[*Handa et al, 1989*]
Xe·6.176H_2O(cr)	7–160 85–270	[*Handa et al, 1986*]
CH_4·5.75H_2O(cr)	85–270	[*Handa et al, 1986*]
NH_4OH(cr)	15–300	[*Chan et al, 1964*]
NH_3·2H_2O(cr)	15–300	[*Chan et al, 1964*]

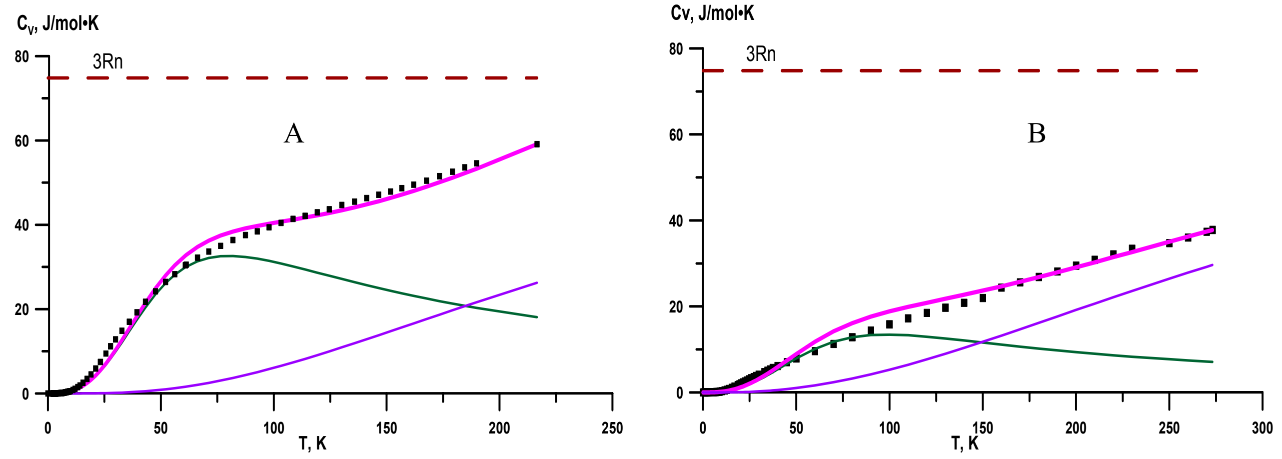

Fig. 1. A – Temperature dependence of heat capacity for CO_2(cr), ■ experiment, Azer-Ainou 2005, ● experiment, [*Manzelii 1971*]. **B** – Temperature dependence of heat capacity for H_2O(cr). ■ experiment, Smith и др 2007, recommended [*Glushko et al, 1978*], ▬calculation by equation (1), ▬ the contribution to the heat capacity, described the first term of equation (1), conventionally designated as L_D, ▬ the contribution to the heat capacity, as described by the second term of equation (1), conventionally designated as L_E, ▬upper limit of the temperature dependence of heat capacity

Table 2. Result of calculation of the equation's (1) coefficients

System	b	c	x	$\alpha_T^2 V_T K_T T$ (J/mol·K)	Δotn%
H_2O(cr)	$2.31\cdot10^{-5}$	$0.10\cdot10^{-4}$	0.0127	1.038	14.6
CO_2(cr)	$0.66\cdot10^{-6}$	$0.18\cdot10^{-4}$	0.003	$1.48\cdot10^{-3}$	4.3
NH_4OH(cr)	$0.29\cdot10^{-5}$	$0.19\cdot10^{-4}$	0.0262	0	8.0

Temperature dependence of the empirical parameter k which changes within the range from 3 to 0, can be presented by the following equation: $k = 9/(9 + xT^2)^{½}$. If $T \rightarrow 0$ and $k = 3$, the first term in square brackets of equation (1) gives the contribution to the heat capacity is described by Debye 's theory ($C_V = AT^3$). If $T > 10$–40 K will become a significant contribution to the heat capacity is described by Einstein's theory [*Khodakovsky, 2012*]. A relative value of both contributions to the value of specific heat, varying with temperature is regulated with the help of k (T).

Today, as a first approximation, to calculate the difference between $Cp - \alpha^2 VTK_T = C_V$ values of α_T, V_T and K_T used at standard temperature, which in the case of crystalline compounds is the melting point of ice. Using equation (1) we carried out calculations for ice, CO_2(cr) and NH_4OH(cr), which are presented in table 2. Unfortunately, we were not able at this stage to find in the literature the data of α_T, V_T and K_T at the standard temperature for the NH_4OH(cr) allow a difference therefore the first phase of work we have taken condition they are equal to zero and put $Cp \approx Cv$. The results of fitting the experimental data for CO_2(cr) and H_2O(cr) are shown in Fig. 1 and 2, as well as the contributions that vary with temperature.

From the data of Tab. 2 the values of relative errors, we see that equation (1) adequately describes the temperature dependence of specific heat CO_2(cr) and NH_4OH(cr), and the calculated values accord with the experimental data. At the same time, for the H_2O (cr) the value of the relative error was very high. However, as can be seen from Fig. 2, the largest deviation values calculated by equation (1), from the experimental data is observed in the range T = 80–150K. Perhaps this is due to the transition of ice in the glassy state in this temperature range, and therefore the complexity of the experiment, as noted by the authors [*Giauque, 1936; Smith, 2007*]. In consequence of this there is doubt that in the interval T = 80–150 K the measured values of heat capacity are in equilibrium.

In conclusion, it should be noted that probability of error will be lower if we use the resulting values for solving the problem of obtaining the enthalpy and entropy which are integral functions in the given range of temperatures.

The work was performed under RAS Presidium Program №22

References:

1. Glushko, V. P, L. Gurevich, G. Bergman. (1978). Thermodynamic properties of individual substances, v. 1, Moscow.
2. Khodakovsky, I. L. (2012). A New Semi-empirical Equations of Temperature Dependences of Heat Capacity and Thermal Expansion Coefficient for inorganic substances, Vestnik ONZ RAN, 4, (doi:).
3. Azger-Ainou, M. (2005). Low-temperature data for Carbon Dioxide, Monatshefte fur Chemie Chemical Monthly, 136, 2017–2027.
4. Chan, J. P., W. F. Giauque (1964). The Entropy of $NH_3\cdot2H_2O$. Heat Capacity from 15 to 300°K, J. Phys. Chem., Vol. 68, N 10, 3053–3057.
5. Chan, J., W. Giauque (1964). Additions and Corrections-The Entropy of $NH_3\cdot2H_2O$. Heat Capacity from 15 to 300 K, J. Phys. Chem., Vol. 68, N 12, 3912/
6. Graham, B. (1969). Heat capacities of O_2, N_2, CO, and NO at low temperatures, Canadian Journal of Physics, 47(1): 23-29, 10.1139/p69–004.
7. Finegold, L, (1969). Low-Temperature Heat Capacities of Solid Argon and Krypton, Phys. Rev., 177, 1383–1391.
8. Jager A., Span R. (2012). Equation of State for Solid Carbon Dioxide Based on the Gibbs Free Energy, J. Chem. Eng. Data, 57, 590–597.
9. Handa, Y. P. (1986). Calorimetric determinations of the compositions, enthalpies of dissociation, and heat

capacities in the range 85 to 270 K for clathrate hydrates of xenon and krypton, J. Chem. Thermodyn., vol. 18, N 10, 891–902.

10. Handa, Y. P, O. Yamamuro, M. Oguni and H. Suga (1989). Low-temperature heat capacities of xenon and krypton clathrate hydrates, J. Chem. Thermodyn., 21, 1249.
11. Handa, Y. P. (1986). Compositions, enthalpies of dissociation, and heat capacities in the range 85 to 270 K for clathrate hydrates of methane, ethane, and propane, and enthalpy of dissociation of isobutane hydrate, as determined by a heat-flow calorimeter, J. Chem. Thermodyn., vol. 18, N 10, 915–921.
12. Giauque, W. F., J. W. Stout (1936). The Entropy of Water and the Third Law of Thermodynamics. The Heat Capacity of Ice from 15 to 273°K, J. Amer. Chem. Soc., vol 58, N 7, 1144–1150
13. Manzhelii, V. G., A. M. Tolkachev (1971). Thermal Expansion, Heat Capacity, and Compressibility of Solid CO_2, Phys. stat. sol. (b) 44, 39.
14. Smith, S. J, B. E. Lang, S. Liu, J. Boero-Goates, B. F. Woodfield (2007). Heat capacities and thermodynamic function of xexagonal ice from T=0.5 K to T=38 K, J. Chem. Thermodynamics, 39, 712–716.
15. Vogt, G. J., K. S. Pitzer (1976). Entropy and heat capacity of methane, spin species conversion, J. Chem. Thermodyn., v. 8, is. 11, p. 1011–1031.

Dorofeeva[1] V. A., Mukhina[2] I. V., Khodakovsky [1,2] I.L. Thermodynamic database for the computer modeling of cosmochemistry and comparative planetology tasks: heat capacity of minerals

[1] V. I. Vernadsky Institute of Geochemistry and Analytical Chemistry RAS, Moscow

[2] Dubna International University of Nature, Society, and Man, Dubna musha08_@mail.ru

Key words: [thermodynamics, modeling, cosmochemistry, the heat capacity of minerals.]

Reference: Dorofeeva, V. A., I. V.Mukhina, I. L.Khodakovsky (2012), Thermodynamic database for the computer modeling of cosmochemistry and comparative planetology tasks: heat capacity of minerals, *Vestnik ONZ RAS, 4, (doi:)*

For a description of the thermodynamic behavior of crystalline materials is necessary to have the equations of the temperature dependence of heat capacity over a wide range of temperatures. The choice of form of these equations, it is advisable to conduct such a way as to meet the maximum limits are theoretical relations and the number of empirical coefficients would be minimal. In this case, these equations can be used not only to interpolate the results of experimental measurements and reasonable extrapolations to the unexplored range of temperatures (usually higher).

The progress in the high-precision measurements of Cp of solids in the wide temperature range allow to propose a simple semi-empirical equation for the lattice heat capacity (Khodakovsky, 2012):

$$C_p = Rn[kL_D + (3 - k)L_E)] + \alpha_T^2 V_T K_T T \qquad (1),$$

where is $L_D = [1 - 1/(1 + bT^3)]$, $L_E = [1 - 1/(1 + cT^2)]$, R – the gas constant, n – number of atoms in the molecule, α_T – thermal expansion coeffcient, V_T – the molar volume, K_T – the bulk modulus, k, b, c – empirical coefficients.

The empirical parameter k varies from 3 to 0. For $k = 3$ and $T \rightarrow 0$ the first term in square brackets of equation (1) gives the Debye equation ($C_V = AT^3$). At $T > 10 - 40$ K, becomes a significant contribution to the heat capacity is described by Einstein's theory.

Semi-empirical equation (1) with reasonable accuracy have reproduced the corresponding experimental points with the smallest number of coefficients and fitting parameters.

Dorofeeva V. A., Mironenko M. V. Conditions of formation of cometary ices

V. I. Vernadsky Institute of Geochemistry and Analytical Chemistry RAS, Moscow dorofeeva@geokhi.ru

Was obtained of the nebula gas phase composition which agree best with the experimentally measured chemical compositionn of Hartley 2 comet.

Key words: [Solar system, evolution, cometary ices]

Reference: Dorofeeva, V. A., M. V. Mironenko (2012), Conditions of formation of cometary ices. *Vestnik* ONZ RAN, 4,

The obtained data for the comet Hartley 2 on isotopic composition of water ice [*Hartogh et al.,* 2012] are evidence to it was evaporated under nebula conditions. At $T \sim 100$ K a hydrogen isotopic composition of ice was changed according to the chemical reaction

$HD_{gas} + H_2O_{gas} \leftrightarrow HDO_{gas} + H_{2\ gas}$, which passes more efficiently in the gas phase than in the heterogenious system "Ice–$H_{2\ gas}$". During next cooling, H_2O_{gas} was condensed into solid clathrate hydrates of various gases. If our assumptions are correct, we can reconstruct a composition of the part of the nebula, where the ice of the comet was formed. Such reconstruction is based on experimental data on composition of Hartley 2 comet [*Meech et al., 2011, Meech et al., 2011; Weaver, 2001; Dello Russo, 2011*] and methods of equilibrium thermodynamics. Variations of *PT* conditions in the nebula at radial distances from Sun ~ 4–10 A.U. according to the model [*Dorofeeva, Makalkin, 2004]* are shown in Fig.1. *PT* conditions of gas hydrates formation from a gas of solar composition are shown in Fig. 2.

The bulk chemical element composition of the nebula was taken as solar abundances according to [*Lodders,* 2010], and a component composition of the gas phase was varied taking into account it's uncertainty. Necessary temperature dependencies of the equilibrium constants of corresponding heterogeneous reactions were derived by summarizing experimental data on conditions of formation of solid gas hydrates and gas ices obtained [*Lunine, Stevenson,* 1985; *Fray et al.*, 2010]. For calculations we used CHEMEQ code [*Mironenko et al.*, 2008], which applies minimization of Gibbs free energy of the system under liner mass-balance restrictions. Some results of calculations are presented in Fig.3.

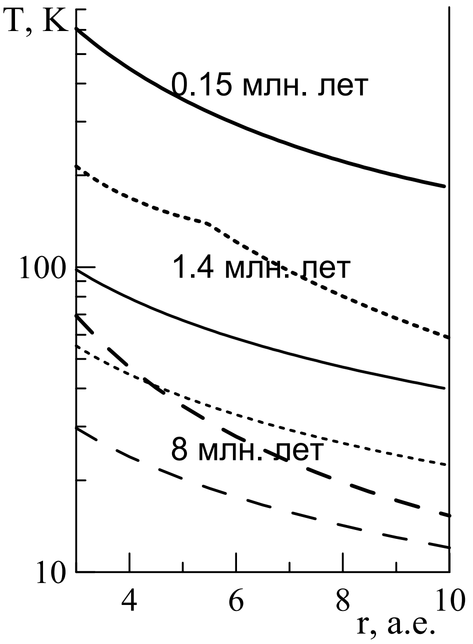

Fig. 1. Variations of *PT* conditions in the nebula at radial distances from Sun ~ 4-10 A.U. Bold lines answer $P = 10^{-6}$ bar, more thin - $P = 10^{-9}$ bar

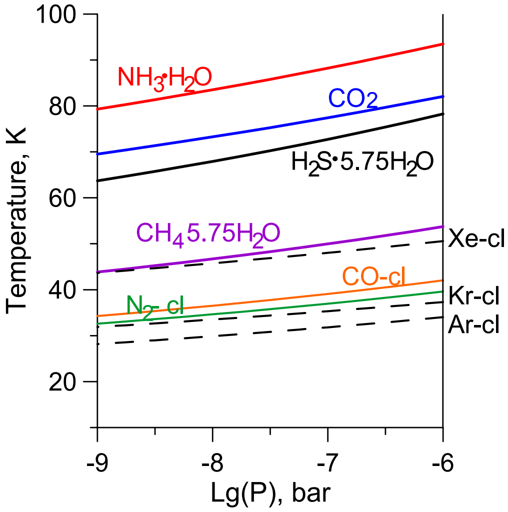

Fig. 2. *PT* conditions of gas hydrates formation from a gas of solar composition according to [*Lunine, Stevenson,* 1985]

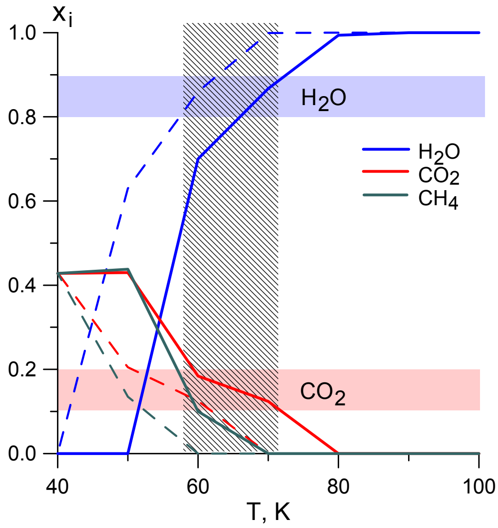

Fig. 3. Variations of the condensed phase composition at the gas phase cooling. Solid lines – correspond the pressure of $P = 10^{-6}$ bar, dashed lines correspond the pressure of $P = 10^{-9}$ bar. Regiong, of H_2O (blue) and CO_2 (pink) correspond the mole phase relations in the comet Hartley 2. The temperature region of stability field of CO_2 and CH_4 clathrate hydrates is shown by dashed lines for pressure interval of $P = 10^{-6}$–10^{-9} bar

As a result of calculations, we obtained C-bearing species ratios of $CO_2 : CO : CH_4 = 1 : 8 : 1$ and N-bering species ratio of $NH_3 : N_2 = 1 : 50$, which agree best with the experimentally measured chemical composition of Hartley 2 comet.

Conclusions. There were regions in Solar nebula, where initially amorphic water ice was evaporated, and as a result of isotopic exchange with $H_{2\ gas}$, it's D/H was significantly decreased.

During next nebula cooling, H_2O_{gas} was condensed as crystal modifications with a possibility of formation of clathrates of various gases under *P-T* conditions of *r* = 4–10 A.U.

Stone-icy bodies (comets) with high contents of volatilities may be formed at near Jupiter orbits, which can be considered as a source of water and other volatilities, including nitrogen, for terrestrial planets.

Probably, the main mechanism of volatilities accumulation in comets, which were formed in Neptunian zone and in Kouiper Belt (*r* > 15–20 A.U.), was their sorption by water ice.

The study was partly supported by RFBR projects 11-05-01137 and 11-05-00780.

References:

1. Brown, P. D., T. J. Millar (1989). Models of the gas-grain interaction-deuterium chemistry. *Mon. Not. R. Astron. Soc.*, 237, 661–671.
2. Dello Russo, N., R. J. Vervack, et al. (2011). The Volatile Composition and Activity of Comet 103P/Hartley 2 During the EPOXI Closest Approach. *The Astrophysical Journal Letters*, v. 734, Iss. 1, article id. L8
3. Fray, N., U. Marboeuf, O. Brissaud, B. Schmitt (2010). Equilibrium Data of Methane, Carbon Dioxide, and Xenon Clathrate Hydrates below the Freezing Point of Water. Applications to Astrophysical Environments. *J. Chem. Eng. Data,* v.55, 5101–5108.
4. Linsky, J. L. (2003). Atomic Deuterium/Hydrogen in the Galaxy. *Space Science Reviews*, v. 106, iss. 1, p. 49–60.
5. Lodders, K. (2010). Solar System Abundances of the Elements. Astrophysics and Space Science Proceedings, Springer-Verlag Berlin Heidelberg, p. 379–417 (ISBN 978-3-642-10351-3).
6. Lunine, J. I., D. J. Stevenson. (1985). Thermodynamics of clathrate hydrate at low and high pressures with application to the outer solar system. *Astrophys. J.* Suppl. 58, 493–531.
7. Meech, K. J., M. F. A'Hearn, J. A. Adams and 194 coauthors. (2011). EPOXI: Comet 103P/Hartley 2 Observations from a Worldwide Campaign. *The Astrophysical Journal Letters*, v. 734, iss. 1, article id. L1.
8. Mironenko, M. V., T. Yu. Melikhova, M. Yu. Zolotov, and N. N.Akinfiev. (2008). "GEOSHEQ_M—A Complex for Thermodynamic and Kinetic Modeling of Geochemical Processes in the Water–Rock–Gas System. Version 2008," *Vestn. ONZ RAN.* 2008. URL: http:/www.scs-is.ru/Russian/cp1251/H_dgggms/1_2008/Informbul_1_2008/Mineral-22.
9. Morbidelli, A. (2012). Dynamical evolution of planetary systems. In "*Planets, Stars and Stellar Systems*", Oswalt, T. D, McLean, I. S.; Bond, H.E.; French, L.; Kalas, P.; Barstow, M.; Gilmore, G. F.; Keel, W. (Eds.), v. 3, 4760 p.
10. Robert, F. (2006). Solar System Deuterium/Hydrogen Ratio. In: *Meteorites and the Early Solar System II* (Space Science

Series) Dante S. L., Harry Y. McSween Jr. (Eds.). Univ. Arizona Press. 942 pp. p. 341–351.

11. Waite, J. H., J. H. Westlake, B. A. Magee, D. T. Young (2009). Titan and Enceladus Composition measured with Cassini INMS and CAPS: Implications for the formation and evolution of the Saturn system. *American Geophysical Union, Fall Meeting 2009,* abstract #P43F-02
12. Weaver, H. A., P. D. Feldman, M. F. A'Hearn, N.Dello Russo, S. A. Stern. (2011). The Carbon Monoxide Abundance in Comet 103P/Hartley 2 During the EPOXI Flyby. *The Astrophysical Journal Letters*, V. 734, Iss. 1, article id. L5.
13. Dorofeeva, V. A., A. B. Makalkin (2004). Evolution of the Early Solar system. Cosmochemical and physics aspects of the problem. M.: Editorial URSS. 288 c.

Dunaeva A.N., Kronrod V.A., Kuskov O.L. Numerical models of Titan's internal structure without the liquid ocean.

V. I. Vernadsky Institute of Geochemistry and Analytical Chemistry, RASciences, Moscow dunaeva@kmail.ru

In this paper models of the internal structure of Titan have been constructed. Conditions for deep water ocean existence depending on the heat flow values through the icy crust of satellite were discussed. It was shown that the internal ocean in Titan can't be formed at the heat flow less 3.3 mW/m^2. At the first stage of this work the possible models of Titan without internal ocean has been built. According to model calculations, it turns out that Titan is a partially differentiated satellite, which in general involves the outer ice shell, rock-ice mantle and inner rock-iron core. The maximum size of the core is 1500 km with a density of rock-iron material 3.62 g/cm^3. Maximum thickness of the external ice shell of Titan reaches 520 km. The total content of H_2O in satellite lies in the range of 45–51 wt. % depending on the rock-iron mantle component density, taken as 3.15–3.62 g/cm^3 respectively.

Key words: [satellites of giant planets, Titan, heat flow, the internal structure]

While studying of Titan, one of the most important key point is understanding history of appearance and evolution of this large icy satellite of Solar System. These studies are associated with attempts to understand the special feature of internal structure of Titan, characteristics of phase and chemical composition of its material.

Basics knowledge's of Titan were obtained during the Cassini-Huygens spacecraft mission aimed at studying the Saturn System. The most important results of this expedition are consists on obtained geophysical data on the mass, mean density and moment of inertia of the satellite.

Analysis of these data allows us to conclude that Titan in many parameters is similar to the Jovian satellite Callisto, whose internal structure discussed in detail in [*Kronrod and Kuskov, 2003; Kronrod and Kuskov, 2005*]. According to these studies, Callisto is partially differentiated satellite, in the depths of which an internal ocean of liquid water up to 150-170 km can possible exists. In respect to the Titan, analysis of all available information does not allow to say definitely whether there are (or not) in its depths some reservoirs of liquid water.

The existence a liquid ocean in satellite interiors depends on the heat transfer processes and temperature distribution over its depth. Possible variants of the radial temperature distribution in Titan, corresponding to different values of heat flow through the satellite's icy crust, shown schematically in Figure 1. The temperature profile of Titan's inner regions was set with the assumption of conductive (in region of low temperatures and pressures at the satellite surface) and convective adiabatic medium typical for the deeper layers of Titan.

As can be seen from the figure, each value of the heat flow corresponds to a specific structure of water-ice shell of Titan (Figure 1 represents a different Titan's models: without internal ocean and with the ocean of intermediate and largest depth). By this means, choice of temperature profile dictates the phase composition (and hence the density distribution) in the water-ice shell of the satellite, and also determines the maximum thickness of its upper icy crust, composed by ice Ih, and the depth of its subcrustal ocean.

In accordance with literature data [*Hussmann et al., 2006*], the heat flux of Titan, defined by its radiogenic heat only, may be equal to 1.18 mW/m^2. Consideration of additional tidal heating gives the value of the heat flow 7.1 mW/m^2 [*Mitri and Showman, 2008*]. In present paper on the base of heat transfer equations and using the water phase diagram all possible values of Titan's heat fluxes have been calculated. Theirs application to Titan leads to variety models of satellite's water-ice shell structure (Fig. 2).

From the Fig. 2 follows that at heat flow less than 3.3 mW/m^2, Titan's internal ocean is not formed. In this case the satellite's outer water-ice shell is represented only by water ice (thickness of the subcrustal ocean (Hw) is equal to zero), whereas under the heat flow equal 7.1 mW/m^2, the outer ice crust up to 80 km and a subcrustal ocean of liquid water up to 315 km can be formed.

In context of this work, the possible models of Titan's internal structure without inner ocean, which correspond to heat flow 3.3 mW/m^2, have been considered. In general case the three-layer model of Titan was constructed. This model includes an outer icy shell, inner rock-iron core and the rock-ice mantle located between them. The special (extreme) cases of this model serves the two-layer models of Titan, including the thick rock-ice layer in combination with either the inner rock-iron core (without an external ice crust), or with an external ice crust, but without the rock core.

To construct the models of Titan's internal structure the following background information was used:

The physical characteristics of the satellite (T, P, gravity acceleration, radius, density, mass, moment of inertia). This parameters form the main restrictions for the developed model.

Geochemical data on density and composition of meteoritic matter (L/LL chondrites). It is suggested that the composition of Titan rock-iron material is corresponds precisely to this matter.

Thermodynamic equations of state for water and high pressure ices.

In compliance with mathematical approach taken in this paper, a model of the internal structure of Titan described by the system of following equations [Kronrod and Kuskov, 2003]:

Equations of hydrostatic equilibrium:

$$\frac{dP}{dR} = -\rho(R)\cdot g(R);$$

$$\frac{dg}{dR} = -4\pi\cdot G\cdot\rho(R) - 2g(R)/R\,, \qquad (1)$$

The equations of the satellite mass and moment of inertia:

$$I = \frac{8}{15}\pi\sum_{i=0}^{n}\rho_i\left(R_i^5 - R_{i+1}^5\right);$$

$$M = \frac{4}{3}\pi\sum_{i=0}^{n}\rho_i\left(R_i^3 - R_{i+1}^3\right), \qquad (2)$$

The equation for calculating ice component concentration in mantle:

$$C_{ice} = \frac{\rho_{ice,m}\left(\rho_{Fe-Si} - \rho_m\right)}{\rho_m\left(\rho_{Fe-Si} - \rho_{ice,m}\right)}, \qquad (3)$$

where *P, R, M, I* – pressure, radius, mass and moment of inertia of Titan, $\rho(R)$ - the density of water-ice shell, $g(R)$ - gravity acceleration, R_i, R_{i+1} – are the greatest and least radii of the *i*th layer with the density ρ_i, $\rho_{ice,m}$ - the ice's average density in mantle, ρ_m - mantle average density, ρ_{Fe-Si} - density of the rock–iron component, C_{ice} - mass fraction of ices in the ice–rock mantle.

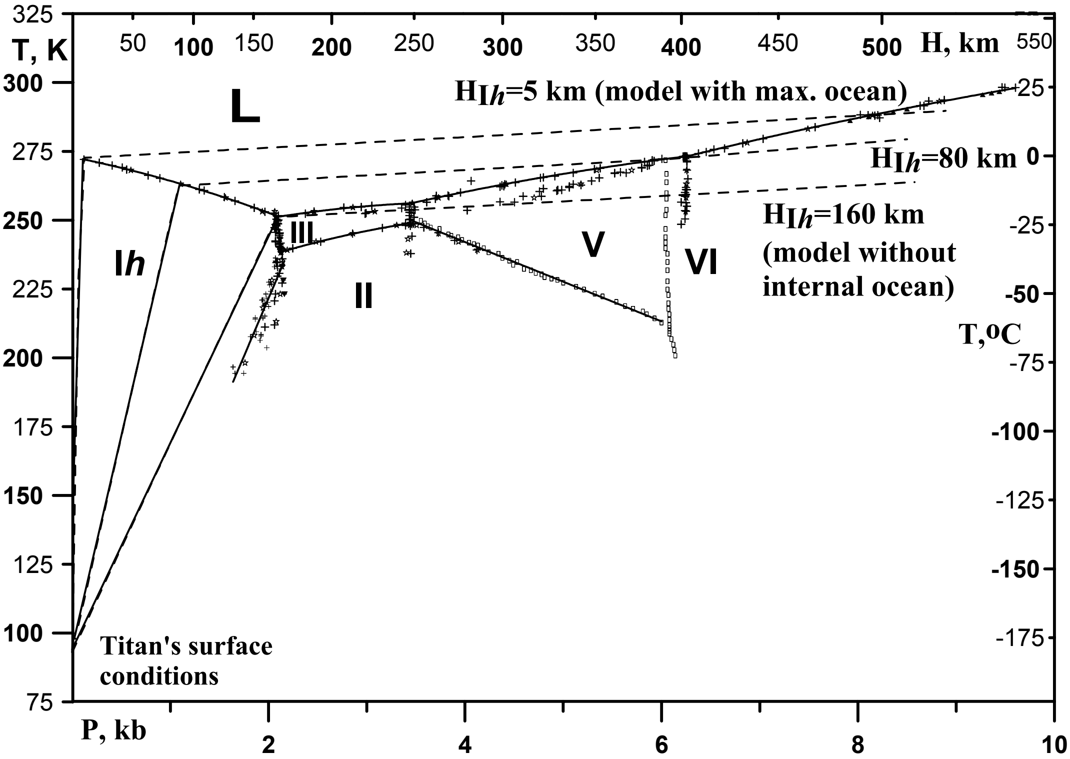

Fig. 1. Phase diagram of water and the distribution of temperature in the Titan's icy crust.
Straight lines - conductive temperature profiles through the external (ice-Ih) crust. The dashed lines – adiabatic convective heat transfer in the water subcrustal ocean and in high-pressure ice medium. H, H_{Ih} - the distance from the satellite's surface (depth) and the thickness of the external ice-I*h* crust.

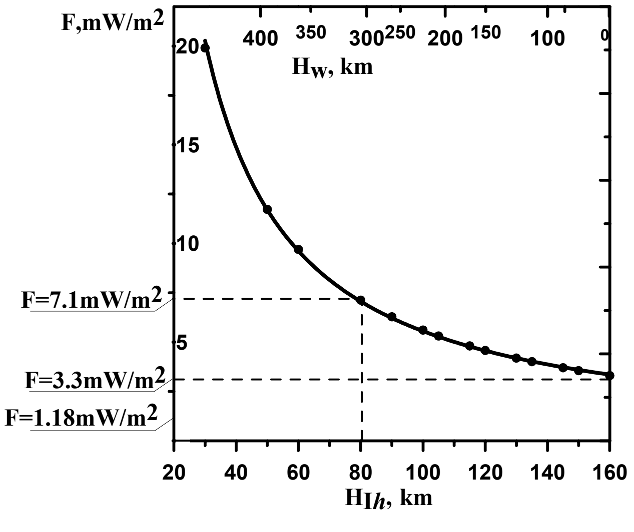

Fig. 2. The thickness of the icy crust of Titan (H_{Ih}) and the thickness of its internal ocean (H_w) via the heat flow through the satellite's ice-I*h* crust.

The system of equations (1-3) is numerically integrated in the range of depths from the surface to the calculated depth of the satellite. In the calculations it was assumed that Titan's rock-iron substance has a constant density with depth. The density of the inner ice-free core was assumed to be 3.62 g/cm^3 in all calculations. Density of *Fe-Si* component in the rock-ice layer of Titan was chosen in the range typical for the ordinary L/LL chondrites with taking into account the silicates hydration: from 3.15 to 3.62 g/cm^3.

Calculations performed by two-layer models of Titan allowed to estimate the maximum size of its outer ice crust and the inner rock-iron core. It was shown that the maximum size of Titan's core achieved through a two-layer model without an external ice shell (Fig. 3a). In this case, partially differentiated Titan is formed. The satellite was represented as inner rocky core with radius of about 1500 km and the outer thick layer of rock-ice material with average density about of 1.4 g/cm^3.

In case when Titan has significant large outer icy crust, its inner rock-iron core not forms, and the interior of the satellite is represented by a homogeneous substance of average density 2.6 g/cm^3, which is likely refer to a mixture of rock material and the high-pressure ice. This structure corresponds to the two-layer model of partially differentiated Titan without inner core (Fig. 3b). On this model the maximum possible thickness of an ice crust reaches 515-520 km at an average density of 1.15 g/cm^3. The mass of water contained in outer ice shell is about 30% of the total mass of Titan.

The phase composition of Titan's icy crust is represented by water ice Ih, III, V, VI, which consistently replacing each other in depth. The upper conductive layer of the icy Ih-crust does not exceed 160 km and has an average density of about 0.94 g/cm^3.

The density of ice in the rock-ice Titan interior varies according to the equations of state and reaches values of 1.77 g/cm^3 at pressures in the center of the satellite equal to 48 kbar (the region of ice VII existence).

A generalized three-layer model of Titan, which differentiated on the icy shell, rock-ice mantle, and rock-iron core, is shown in Fig. 4. In this model many varieties of the internal structure of the satellite are realized. All models differ in the thickness of outer ice shell, and concurrently with it the size of the inner rock core, as well as the size and density of the rock-ice mantle are also changing.

The total content of ice in Titan was determined by its summary concentration in the outer ice shell and in the rock-ice mantle. The calculations have shown that the bulk amount of ice in the satellite is strongly depended on the density of the mantle rock component and less on extent on the thickness of outer water-ice shell.

In the two-layer models of Titan with a minimal thickness of an ice crust and the density of Fe-Si component 3.15 - 3.62 g/cm^3, the mass fraction of ice in the satellite is 49.5 - 50.6 wt. %, respectively. At the maximum size of an ice shell allowable range of the ice content in Titan increases, respectively, to 45.1–51.1 wt. %.

Thus, for a whole range of Titan possible models the total water content in satellite is placed in the range from 45 to 51 wt. %.

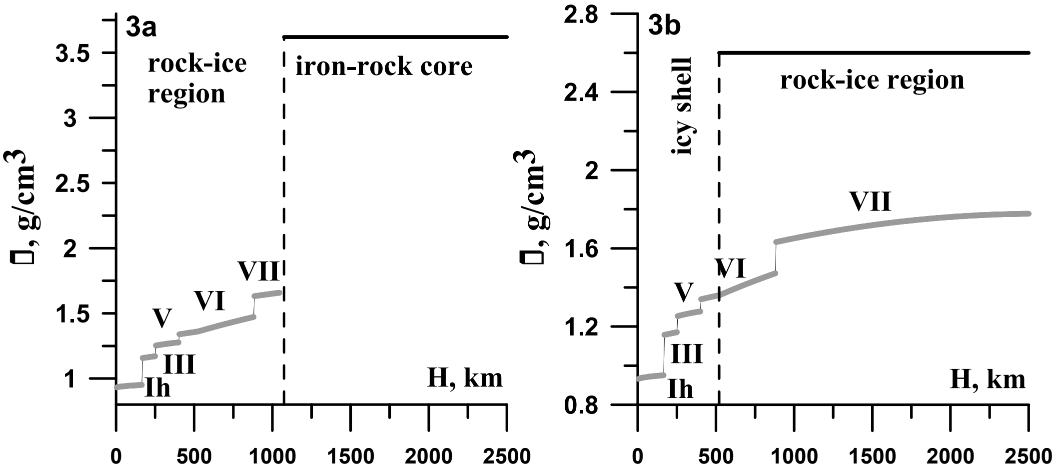

Fig. 3. Two-layer models of Titan: 3a - a model with a maximum rock-iron core, 3b - a model with a maximum ice crust. Gray lines show the change in ice density in the ice crust and in the rock-ice region

.

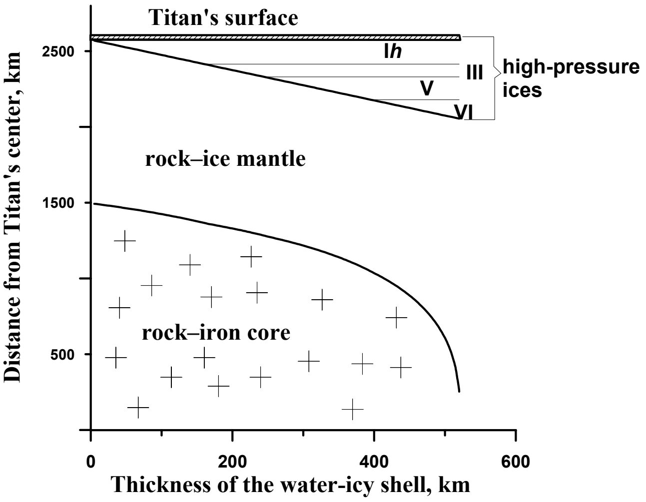

Fig. 4. A general model of Titan's internal structure without subcrustal ocean.

This research was supported by Russian Academy of Sciences under Programs 22, and by RFBR grant 12-05-00033.

References:

1. Kronrod, V. A., Kuskov, O. L. (2003) Chemical differentiation of the Galilean satellites of Jupiter: 1. An internal structure of Callisto's water-ice shell, *Geokhimia*, № 9, pp. 968-983.
2. Kronrod, V. A., Kuskov, O. L. (2005) Chemical differentiation of the Galilean satellites of Jupiter: 3. Models of the Callisto internal structure, *Geokhimia*, № 4, pp. 1-15.
3. Hussmann, H. et al. (2006) Subsurface oceans and deep interiors of medium-sized outer planet satellites and large trans-neptunian objects, *Icarus,* V. 185, pp. 258–273.
4. Mitri, G., Showman, A. P. (2008) Thermal convection in ice-I shells of Titan and Enceladus, *Icarus*, V. 193, pp. 387–396.

Ivliev A.I., Kuyunko N. S. Thermoluminescence and metamorphism of CO and CV carbonaceous chondrites

Vernadsky Institute of Geochemistry and Analytical Chemistry
RAS, Moscow cosmo@geokhi.ru

The purpose of the present paper was study of metamorphism carbonaceous chondrites on TL-device of GEOCHI RAS with usage of the scale linking value of a subtype to intensity of glow curve TL. These results have shown good coincidence of carbonaceous chondrite subtypes, obtained by us and in other laboratories.

Key words: [thermoluminescence, carbonaceous chondrites, metamorphism]

Citation: Ivliev, A.I., Kuyunko N.S. (2012), Thermoluminescence and metamorphism of CO and CV carbonaceous chondrites, *Vestnik ONZ RAS, 4, (doi:)*

Introduction

The CO chondrites are similar to type 3 ordinary chondrites in several respects [*Sears et al.,* 1991]. They are both chondritic in bulk composition, with non-volatile elemental abundances generally within about 30% of the CI values. Thus the two groups are mineralogically very similar, consisting of olivine, pyroxene, plagioclase, metal and sulfide. Like the ordinary chondrites the CO chondrites appear to constitute a metamorphic sequence [*McSween*, 1977a, *Keck and Sears,* 1987; *Scott and Jones,* 1990]. However, they also differ from ordinary chondrites in several respects. They are isotopically different [*Clayton et al.,* 1976, *Clayton and Mayeda,* 1984], element ratios show small but significant differences [*Anders et al*., 1976, *Kallemeyn, Wasson,* 1981], they contain refractory amoeboid inclusions, and their chondrules are smaller [*McSween*, 1977a, *Rubin,* 1989]. Unlike type 3 ordinary chondrites, CO chondrites often contain primary calcic feldspar [*Van Schmus,* 1969], presumably associated with the refractory inclusions. Keck and Sears [*Keck and Sears,* 1987] also found that the thermoluminescence (TL) sensitivity of the (110-120)°C peak increased by a factor of 100 with increasing metamorphism, while the TL sensitivity of a second TL peak at 230°C was not metamorphism-dependent. They suggested that the first peak was caused by feldspar formed by devitrification of chondrule glass, a situation analogous to that of type 3 ordinary chondrites [*Guimon et al.,* 1985, *Guimon et al.,* 1988], while the 230°C peak was due to primary (i.e. non-metamorphic) feldspar, perhaps associated with refractory inclusions.

Compositional equilibration between refractory inclusions and the ferromagnesian components, and variations in the homogenization of matrix olivines, suggests that the CV chondrites have suffered various levels of parent-body metamorphism [*McSween,* 1977b, *Peck,* 1984, *Scott et al.,* 1988]. Since the CV chondrites consist of both oxidized and reduced subgroups, a single metamorphic series is precluded although two parallel series are possible [*McSween,* 1977b]. The petrographic, mineralogical and bulk compositional differences among the CV chondrites indicate the TL sensitivity of the ~ (110-130) °C TL peak is reflecting the abundance of ordered feldspar, especially in chondrule mesostasis, which in turn reflects parent-body metamorphism [*Guimon R.K., et al.,* 1995].

The purpose of the present paper was study of metamorphism CO and CV chondrites on TL-device of GEOCHI RAS with usage of the scale linking value of a subtype to intensity of glow curve TL, proposed [*Sears et al.,* 1991, *Guimon R.K., et al.,* 1995].

Experimental

The measuring induced by X-rays TL in 21 samples of carbonaceous chondrites carried out, composition which one included following types: CO3 - 9, CV3 - 8 and CK - 4 samples. Samples, is weight from 0.7 up to 1.0 g, were broken up and are crushed to jasper mortar box. The magnetic fraction was removed with the help of a manual magnet. From a non-magnetic fraction was ready till three probes of each sample is weight on 2 mg. After measuring natural TL (the heating up to 500 ^{O}C), samples were irradiated with X-rays within two minutes and then induced TL was measuring. The device for measuring TL, preparation of samples and requirements of an irradiation are in more detail described in [*Ivliev et al.,* 1995, 1996, 2002].

Results and conclusions

The results of measured induced TL in investigated samples of carbonaceous meteorites are listed in table, where I_{TL} - peak height TL at the temperature of about 130 ^{O}C. The value of I_{TL} was gauged rather I_{TL} of a meteorite Dhajala, assumed for 1. In a column "Others" the boundaries of measuring of a subtype obtained as both TL and other methods [*Sears et al.,* 1991, *Guimon R.K., et al.,* 1995]. By symbol (*) are marked the recommended petrographic type. In a fig. 1 the glow curves of TL of carbonaceous meteorites of different types CO, CV and CK are shown. Large part of the investigated meteorites has the composite shape of glow curves with peaks in the field of temperature: (110-130) ^{O}C and, as a rule, some peaks in field > 150^{O}C. The exception compounds only meteorite Coolidge, shown only peaks in field ~ 130 ^{O}C and ~ 150 ^{O}C (fig. 2). Such shape of TL peaks is most typical for glow curves of ordinary chondrites [*Newton et al.,* 1995].

Table. Observed results of a peak height (I_{TL}) of glow curves (130 ^{O}C) and degree of metamorphism carbonaceous chondrites

Meteorite	Type	I_{TL} (I_{TL} Dhajala=1)	Subtype	
			This paper	Others
Felix	CO	0.106	3.4	3.2-3.5 (3.4*) [*Sears et al.,* 1991]
Isna	CO	0.356	3.6	3.6-3.8 (3.7*) [*Sears et al.,* 1991]
Kainsaz	CO	0.245	3.5	3.1-3.5 (3.2*) [*Sears et al.,* 1991]
Lancé	CO	0.200	3.5	3.4-3.7 (3.4*) [*Sears et al.,* 1991]
Ornanć	CO	0.077	3.3	3.3-3.6 (3.4*) [*Sears et al.,* 1991]
Warrenton	CO	0.342	3.6	3.5-3.8 (3.6*) [*Sears et al.,* 1991]
Allende	CV	0.145	3.4	3.1-3.6 (3.2*) [*Guimon R.K., et al.,* 1995]
Axtell	CV	0.008	3.0	3.0-3.3 (3.0*) [*Guimon R.K., et al.,* 1995]
Coolidge	CV	0.913	3.7	3.8->3.8 (3.8*) [*Guimon R.K., et al.,* 1995]
Efremovka	CV	0.070	3.3	3.0-3.6 (3.2*) [*Guimon R.K., et al.,* 1995]
Grosnaja	CV	0.022	3.1	3.0-3.3 (3.3*) [*Scott et al.,* 1988]
Leoville	CV	0.060	3.3	3.0-3.6 (3.0*) [*Guimon R.K., et al.,* 1995]
Acfer 202	CO	0.079	3.3	3.5 [*Newton et al.,* 1995]
Dar Al Gani 303	CO	0.044	3.2	—
Dar Al Gani 078	CO	0.059	3.3	—
C4V3 N13^{+}	CV	0.030	3.2	—

Meteorite	Type	I_{TL} (I_{TL} Dhajala=1)	Subtype	
			This paper	Others
CVII-3$^+$	CV	0.171	3.5	—
Dhofar 015	CK	0.212	3.5	—
Karoonda	CK	0.008	3.0	—
Maralinga	CK	0.013	3.0	—
Ningqiang	CK	0.029	3.1	—

+ - Working title of a meteorite. (*) - Recommended petrographic type.

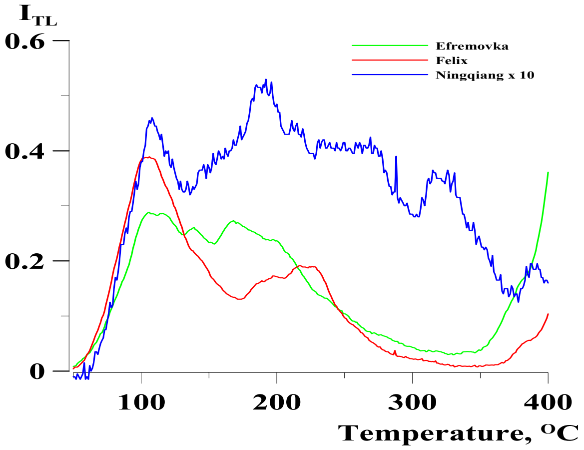

Fig. 1. Glow curves of CO, CV, and CK chondrites

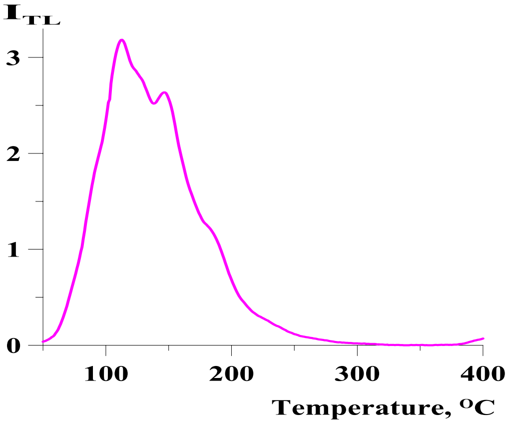

Fig. 2. Glow curve of Coolidge CV chondrite

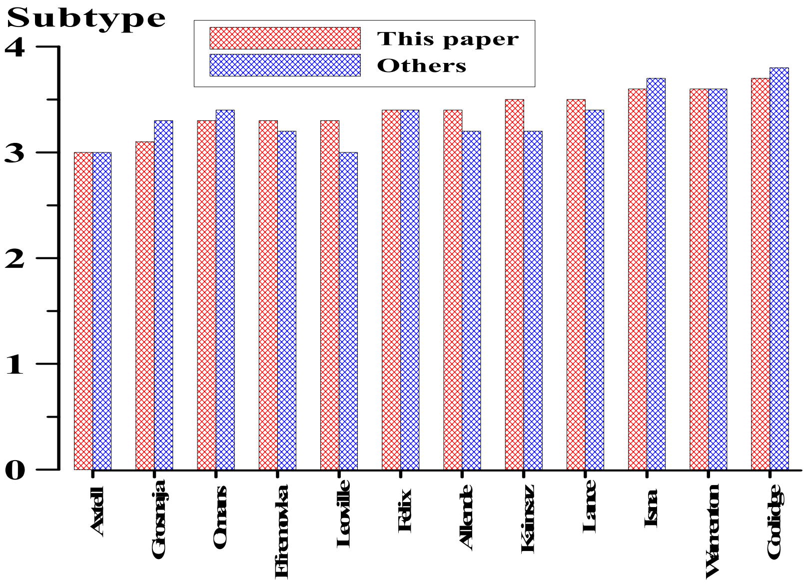

Fig. 3. Comparison of observed data of a metamorphism degree of carbonaceous meteorites investigated in different labs

For check out of device and the procedures of examination of a degree of metamorphism carbonaceous chondrites were carried out measuring in 12 meteorites, samples which one coincide with studied in papers [*Sears et al.,* 1991, *Guimon R.K., et al.,* 1995]. These results, reduced in the table and in a fig. 3, have shown good coincidence of carbonaceous chondrite subtypes, obtained by us and in other laboratories. The obtained results testify that the method of TL measurement, applied by us, is suitable for study of a degree of metamorphism carbonaceous chondrites. On this basis the subtypes three CO chondrites were studied: Acfer 202, Dar Al Gani 078, Dar Al Gani 303, taking place in a collection of meteorites GEOCHI RAS, and two CV chondrites recently entered a collection: C4V3 N13 and CVII-3. The received values of subtypes are well compounded with the data of petrographic and other investigations. Besides, the measurings in four samples CK chondrites are carried out: Dhofar 015 -CK3, Ningqiang - CK - ungr: Karoonda - CK4 and Maralinga - CK4. The obtained results indicate, that the CK chondrites are unique among metamorphosed chondrites in showing no detectable induced TL, which is consistent with literature data that suggests very unusual feldspar in these meteorites.

References:

1. Anders, E., H. Higuchi, R. Ganapathy, J. W. Morgan (1976). Chemical fractionations in meteorites—IX. C3 chondrites, Geochim. Cosmochim. Acta, v. 40, p.1131–1139.
2. Clayton, R. N., et al. (1976). A classification of meteorites based on oxygen isotopes, Earth Planet. Sci. Lett., v. 30, p. 10–18.
3. Clayton, R. N., T. K. Mayeda (1984). The oxygen isotope record in Murchison and other carbonaceous chondrites, Earth Planet. Sci. Lett., v. 67, p. 151–161.
4. Guimon, R. K., B. D. Keck, K. W. Weeks, J. De Hart, D. W. G. Sears (1985). Chemical and physical studies of type 3 chondrites—IV: Annealing studies of a type 3.4 ordinary chondrite and the metamorphic history of meteorites, Geochim. Cosmochim. Acta, v. 49, N7, p.1515–1524.
5. Guimon, R. K., G. E. Lofgren, , D. W. G. Sears (1988). Chemical and physical studies of type 3 chondrites. IX: Thermoluminescence and hydrothermal annealing experiments and their relationship to metamorphism and aqueous alteration in type <3.3 ordinary chondrites, Geochim. Cosmochim. Acta, v. 52, N1, p. 119–127.

6. Guimon R. K., S. J. Symes, D. W. G. Sears, P. H. Benoit (1995). Chemical and physical studies of type 3 chondrites XII: The metamorphic history of CV chondrites and their components, Meteoritics, v. 30, N6, p. 704–714.
7. Ivliev, A. I., D. D. Badyukov, L. L. Kashkarov (1995). Study of Thermoluminescence in Samples Subjected to Experimental Shocked Samples. I: Oligoclase, Geokhimiya, No. 9, p.1368–1377.
8. Ivliev, A. I., D. D. Badyukov, L. L. Kashkarov, L. L. (1996). Investigations of Thermoluminescence in Experimentally Shocked Samples: II. Quartz, Geokhem. Int. v. 34, p. 912–919.
9. Ivliev, A. I., D. D. Badyukov, N. S. Kuyunko, E. A. Kozlov (2002). A Study of Thermoluminescence in Experimentally Shocked Samples. III: Calcite, Geochem. Int. v. 40, p. 739–750.
10. Kallemeyn, G. W., J. T. Wasson (1981). The compositional classification of chondrites—I. The carbonaceous chondrite groups, Geochim. Cosmochim. Acta, v. 45, N7, p.1217–1230.
11. Keck, B. D., D. W. G. Sears (1987). Chemical and physical studies of type 3 chondrites—VIII: Thermoluminescence and metamorphism in the CO chondrites, Geochim. Cosmochim. Acta, v.51, p. 3013–3021.
12. McSween, H. Y. (1977a). Carbonaceous chondrites of the Ornans type: A metamorphic sequence, Geochim. Cosmochim. Acta, v.41, p. 477–491.
13. McSween, H. Y. (I977b). Petrographic variations among carbonaceous chondrites of the Vigarano type, Geochim. Cosmochim. Acta, v. 41, N12, p.1777–1790.
14. Newton, J., M. A. Sephton, C. T. Pillinger (1995). Contamination differences between co3 falls and antarctic and saharan finds: a carbon, Workshop on Meteorites from Cold and Hot Deserts, LPI Tech. Rpt. 95-02, p.51–53.
15. Peck, J. A. (1984). Origin of the variation in properties of CV3 meteorite matrix and matrix clasts, Lunar Planet. Sci. 15, p. 635–636.
16. Rubin, A. E. (1989). Size-frequency distributions of chondrules in CO3 chondrites, Meteoritics, v. 24, N 3, p. 179–189.
17. Sears, D. W. G., J. D. Batchelor, J. Lu, B. D. Keck (1991). Metamorphism of CO and CO-like chondrites and comparison with type 3 ordinary chondrites, Proc. NIPR Symp. Antarct. Meteorites, N4, p. 319–343.
18. Scott, E. R. D., R. H. Jones (1990). Disentangling nebular and asteroidal features of CO3 carbonaceous chondrite meteorites, Geochim. Cosmochim. Acta, v. 54, p.2485–2505.
19. Scott, E. R. D., D. J. Barber, C. M. Alexander, R. Hutchinson, J. A. Peck (1988). Primitive material surviving in chondrites - Matrix In: Meteorites and the Early Solar system, eds: Kerridge, J. F. & Matthews, M. S., Univ. Arizona Press, Tucson, p. 718–745.
20. Van Schmus, W. R. (1969). Mineralogy, petrology, and classification of types 3 and 4 carbonaceous chondrites. In: Meteorite Research, ed.: P. M. Millman, Dordrecht, D. Reidel, Holland, 480–491.

Karakin[1] A.V., Lebedev[2] E. B., Pokatashkin[1] P. A. Possible mechanism of beginnings of the Lunar core and crust

[1]State Scientific Center of Russian Federation VNII Geosystem, Moscow

[2]V. I. Vernadsky Institute of Geochemistry and Analytical Chemistry of RAS, Moscow *avkarakin@gmail.com*

A conceptually new model of compaction is introduced. The key innovative factor in the model is the appraisal of the presence of a multi-phase fluid. We apply the model to a lunar iron core formation hypothesis to test the theoretical possibility of its genesis through iron sinking from magmatic lakes.

Key words: [compaction, two-phase compaction, Lunar iron core formation.]

Reference: Karakin, A. V., E.B. Lebedev, P.A. Pokatashkin (2012), Possible mechanism of beginnings of the Lunar core and crust, *Vestnik ONZ RAN, 4,*

We examine the formation mechanism of the Earth-group planets' iron core at the initial stage of its formation, assuming that at the initial stage (partly-melt condition) planets were intensely collided by huge meteorites and asteroids. "Lakes" of melt matter appeared on the surface of the planets after such collisions. Due to the process of differentiation that took place at those magmatic lakes, iron with addition of some other metals sunk to the bottom. At this stage of planet formation its temperature was rather high (~1450^0C) and was near the solidus of peridotites. The melting point of iron is about 100^0 higher. Iron is warming the environment with the gravitation energy due to viscous friction while shrinking. That's why iron is going to the centre of the moon, being melt. By the way, lighter silicate fractions of peridotites are going up along the melted channels.

In the inner layers of the planet some physical parameters could change, so we are taking into consideration only the near-surface layer. We connect parameters with the Moon, but this model could be applied to other planets of the Earth group. At this region process of two-phase compaction takes place [*Karakin, 2005*]. One-dimensional approximation could be considered. On Earth such mechanism is still working in the mid-ocean ridges with the basalt layer formation of ocean crust.

Heavier iron (and its alloys) moves significantly faster than silicates. That's why duration of the iron core formation is short compared to cosmic scales (hundreds of millions of years).

Non-isothermal model of two-phase compaction is considered (two liquid phases are melts of iron and magmatic silicate and quasi-solid skeleton silicon phase). Phase transition between silicate phases is possible. Let's name r and f the density and porosity of porous viscous matter.

Values that belong to the whole matter would be left without indexes. Values with upper indexes *(o)* and *(k)*, (where $k=s, f$) belongs to skeleton and liquid silicate and iron phases.

Let's write the Terzaghi relation and the force balance equation:

$$s_{ij} = s^{ef}_{ij} - pd_{ij} . \qquad (1)$$

$$\frac{\P s_{ij}}{\P x_j} + r g_i = 0 . \qquad (2)$$

$$\sigma^{ef}_{ij} = \eta\left(\frac{\partial w_i}{\partial x_j} + \frac{\partial w_j}{\partial x_i} - \frac{2}{3}\frac{\partial w_k}{\partial x_k}\delta_{ij}\right) + \zeta\frac{\partial w_k}{\partial x_k}\delta_{ij} . \qquad (3)$$

where s_{ij}, s^{ef}_{ij} – are full and effective stress tensors, p – porous pressure, $\overset{1}{w}$ –skeleton velocity, z and h – coefficients of volume and shear viscosity, $\overset{1}{g}$ – gravitation acceleration. Let's add the equations of continuity of mass for each phase and the Darci's law for each liquid phase.

$$\frac{\partial}{\partial t}\left[(1-f)\rho^{(0)}\right] + div\left[(1-f)\rho^{(0)}\vec{w}\right] = -Q . \qquad (4)$$

$$\frac{\partial}{\partial t}\left(\rho^{(s)}f^{(s)}\right)+div\left(\rho^{(s)}\vec{v}^{(s)}\right)+div\left[\rho^{(s)}f^{(s)}\vec{w}\right]=Q,$$
$$\frac{\partial}{\partial t}\left(\rho^{(f)}f^{(f)}\right)+div\left(\rho^{(f)}\vec{v}^{(f)}\right)+div\left[\rho^{(f)}f^{(f)}\vec{w}\right]=0. \qquad (5)$$

$$gradp=-\frac{\eta^{(k)}}{k^{(k)}}\vec{v}^{(k)}+\rho^{(k)}\vec{g},\ k=s,f, \qquad (6)$$

where $\vec{v}^{(k)}$ – partial filtration velocity, $\eta^{(k)}$ – coefficient of viscosity of fluid phases, $k_p^{(k)}$ – coefficient of absolute phase permeability of *k*-phase, Q – mass source density (transition between silicate phases). Due to process' logic, taken at micro-level of elementary volume all phase pressures are equal.

Values ζ, η are in general functions of porosity and invariants of tensors of stress and velocity of deformation. In linear rheology case, those values depend only from porosity. Let's separate filtration and hydrostatic components in porous pressure: $p=\tilde{p}+p^{G},\quad p=\tilde{p}+p^{G},\quad gradp^{G}=\rho^{(0)}\vec{g}$ .Thus the equation of filtration (6) would reduce to:

$$grad\tilde{p}=-\frac{\eta^{(k)}}{k^{(k)}}\vec{v}^{(k)}+\Delta\rho^{(k)}\vec{g},\ \text{where}\ k=s,f,$$
$$\Delta\rho^{(k)}\equiv\rho^{(k)}-\rho^{(0)}. \qquad (7)$$

Value $\Delta\rho^{(k)}$ has sense of phase density difference. Equations (1) – (7) could be modified to a form of equations of motion with skeleton velocity

$$grad\left[\left(\zeta+\frac{1}{3}\eta\right)div\vec{w}\right]+\eta\nabla^{2}\vec{w}=gradp-\rho\vec{g}. \qquad (8)$$

With (7) equation (8) could be modified to

$$grad\left[\left(\zeta+\frac{1}{3}\eta\right)div\vec{w}\right]+\eta\nabla^{2}\vec{w}=-\frac{\eta^{(f)}}{k^{(f)}}\vec{v}^{(f)}+\left(1-f^{(f)}\right)\Delta\rho^{(f)}\vec{g}-f^{(s)}\Delta\rho^{(s)}\vec{g}$$
$$grad\left[\left(\zeta+\frac{1}{3}\eta\right)div\vec{w}\right]+\eta\nabla^{2}\vec{w}=-\frac{\eta^{(s)}}{k^{(s)}}\vec{v}^{(s)}+\left(1-f^{(s)}\right)\Delta\rho^{(s)}\vec{g}-f^{(f)}\Delta\rho^{(f)}\vec{g}. \qquad (9)$$

Due to low porosity equation (9) could be reduced to

$$grad\left[\left(\zeta+\frac{1}{3}\eta\right)div\vec{w}\right]+\eta\nabla^{2}\vec{w}=-\frac{\eta^{(f)}}{k^{(f)}}\vec{v}^{(f)}+\Delta\rho^{(f)}\vec{g}$$
$$grad\left[\left(\zeta+\frac{1}{3}\eta\right)div\vec{w}\right]+\eta\nabla^{2}\vec{w}=-\frac{\eta^{(s)}}{k^{(s)}}\vec{v}^{(s)}+\Delta\rho^{(s)}\vec{g}. \qquad (10)$$

Let's modify equations of continuity (4), (5), assuming that phase density are constants,

$$\frac{\partial f^{(s)}}{\partial t}+div\left(\vec{v}^{(s)}+f^{(s)}\vec{w}\right)=\frac{Q}{\rho^{(s)}},$$
$$\frac{\partial f^{(f)}}{\partial t}+div\left(\vec{v}^{(f)}+f^{(f)}\vec{w}\right)=0,$$
$$-\frac{\partial f}{\partial t}+div(1-f)\vec{w}=-\frac{Q}{\rho^{(0)}}. \qquad (11)$$

Particularity of compaction equations (10–11) is based on the presence of some kind of medium's own size, called compaction length:

$$H\equiv\sqrt{\frac{\zeta*k}{\eta}}.$$

If characteristic zone of motion scale significantly differs from compaction length, compaction equations degenerate and medium transforms to another state. Having two-phase fluid leads to two peculiar phases' compaction length

$$H^{(k)}\equiv\sqrt{\frac{\zeta*k^{(k)}}{\eta^{(k)}}}. \qquad (12)$$

In such case phase equation degeneration could happen. In other words, degeneration by one phase doesn't mean degeneration by another. Viscosity of iron and silicates differs by two orders. According to the introduction, the porous space structure and partial volumes of both liquid phases are nearly equal. This leads to the fact that the phase permeability is also nearly equal.

$$k^{(s)}=k^{(f)}\equiv k.$$

That means compaction length of iron and silicate differs by one order (see (12).

$$\frac{H^{(f)}}{H^{(s)}}=\sqrt{\frac{\eta^{(s)}}{\eta^{(f)}}}=10. \qquad (13)$$

Using (13) makes it clear that compaction length of liquid phases differs significantly. The main point of all facts is heavy iron phase down movement due to ascending force. Silicate upwards migration is only a concomitant process. Compaction length at silicate matters of asthenosphere is about 200-300 m (at depth c.a. 100km). Assuming this and using (13) compaction length of iron phase is c.a. 3km, with the help of Darci's Law (6) phases filtration relation can be obtained.

$$\frac{\eta^{(f)}v^{(f)}}{\Delta\rho^{(f)}}=\frac{\eta^{(s)}v^{(s)}}{\Delta\rho^{(s)}},\quad \frac{v^{(f)}}{v^{(s)}}\approx 10^{3}. \qquad (14)$$

Knowing some other data we can obtain absolute phase velocities:

$$v^{(f)}\approx\frac{k^{(f)}\Delta\rho^{(f)}g_{lun}}{\eta^{(f)}}\approx 10\text{m/year},\quad v^{(s)}\approx 10\text{cm/year}$$

$$v^{(k)}=\left|\vec{v}^{(k)}\right|.$$

Iron phase moves 1000 times faster than silicate (14), assuming this the compaction equation could be reduced to one-phase compaction with only iron fluid phase (silicate fluid phase could be included into skeleton phase). After filtration downwards or incrusting of iron, compaction of silicate fluid could be taken into account. Thus, compaction with two-phase fluid splits into two independent compaction processes with one fluid phase [McKenzie D. 1984, Karakin A.V. 1999]. Firstly, iron phase moves downwards significantly more fast and intensively, than silicate fluid phase filtrates upwards.

Results obtained higher could be discussed in frame of the core formation hypothesis by sinking of iron from magmatic lakes to the planet center. Lateral dimension is rather big (1mm). This means that iron could move through these channels though it doesn't wet silicate matters. At the front of motion iron is enshrouded by melt silicate and partial pores pressures are equal. At this stage silicate phase could be viewed as static. As soon as iron has migrated, silicate phase begins to move upwards. Both phases movement occurs independently within different channels with different velocities and partial porous pressures.

Gravity decreases linearly with depth till zero at the center. So, at rather low depths compaction mechanism as the main factor of iron sedimentation strictly weakens and another one takes place. Numerical calculations for each model with one-phase fluid were provided. They showed that wave packages have a tendency to collapse and create clear melt lenses while moving. Cameras of iron melt after getting critical size can break down (due to Rayleigh-Tailor instability) and create iron core. Later accompanied fact upwards migration of silicate melt takes place. It can be described as one-phase fluid compaction. This occurs much more slowly but with similar patterns. Particularly, wave packages could collapse and create volcano eruptions. Lunar volcanoes could have such origin.

References:

1. Karakin A. V. (2005). Compaction with a Multiphase Fluid, *Fizika Zemli. № 9*. pp. 12–20.
2. McKenzie, D. (1984), The generation and compaction of partially molten rock, *Journal of Petrology.* v. 25, № 3, pp. 713-765.
3. Karakin, A. V. (1999). The General Theory of Compaction at a Small Porosity, *Fizika Zemli.* № 12. C. 13-26. (in Russian). *Izvestiya, Phys. Solid Earth*, vol. 35, pp. 977 – 989 (in English).

Korochantseva[1] E. V., Buikin[1] A. I., Lorenz[1] C. A., Korochantsev[1] A. V., Trieloff [2]M. Argon isotope geochemistry in gas-rich regolith breccia Dhofar 018

[1]Vernadsky Institute of Geochemistry and Analytical Chemistry RAS, Moscow

[2]Institute of Geosciences, Heidelberg University, Germany

bouikine@mail.ru

Key words: [argon cosmochemistry, ^{40}Ar-^{39}Ar-dating, regolith breccia]

Reference: Korochantseva, E. V., A. I. Buikin, C. A. Lorenz, A. V. Korochantsev, M. Trieloff (2012), Argon isotope geochemistry in gas-rich regolith breccia Dhofar 018, *Vestnik ONZ RAN, 4, doi:*

Dhofar 018 is a typical howardite mainly composed of eucritic and diogenitic lithologies. This meteorite contains a wide variety of foreign components, some of which were not known to occur in howardites so far, e.g., LL-chondrite and aubrite clasts. Howardites (as HED meteorites in general) are potentially informative of impact cratering events, in particular the late heavy bombardment ~4 Ga ago, and frequently preserve records of exposure to solar corpuscular radiation. Here we report the first results of ^{40}Ar-^{39}Ar analyses of Dhofar 018 mineral separates and whole rock sample. Dhofar 018 whole rock (WR) has the highest concentrations of ^{36}Ar and ^{38}Ar (485 and 94×10^{-8} cm^3 STP/g, respectively) found so far in howardites. ^{36}Ar/^{38}Ar ratios in individual temperature extractions are generally >5, with a maximum ^{36}Ar/^{38}Ar value of 5.35±0.04 at 760°C. This ratio likely implies a higher ^{36}Ar/^{38}Ar value of the trapped endmember composition, as Dhofar 018 experienced a significant exposure history and ^{37}Ar derived from Ca – the main target element for ^{38}Ar production – is released at this temperature. Evidently, this breccia contains solar wind implanted Ar similar to other howardites. The cosmic ray exposure age of Dhofar 018 (WR) crucially depends on the uncertainty of the solar wind argon isotopic composition. Assuming the solar wind ^{36}Ar/^{38}Ar value as high as 5.8 the cosmic ray exposure age would be ~100 Ma, while a ^{36}Ar/^{38}Ar ratio of 5.35 would imply ~31 Ma. Meanwhile our data indicate that Dhofar 018 had a pre-compaction exposure: The cosmic ray exposure age of a coarse-grained plagioclase separate is only ~13 Ma and independent on different possible (^{36}Ar/^{38}Ar)$_{\text{trapped}}$ values due to the high fraction of ~90 % of ^{38}Ar$_{\text{cos}}$. Hence, this rock resided for a long time on the surface of its parent body, acquiring solar wind and cosmogenic gases, allowing incorporation of projectile matter ranging from reduced (enstatite type) to oxidized (carbonaceous type) material. As the coarse-grained plagioclase separate released only negligible amounts of solar argon, an isochron analyses could be applied and revealed the presence of a trapped argon component at >660°C with a ^{40}Ar/^{36}Ar ratio of <400. Correcting the age spectrum for this non-solar extraterrestrial component results in a partial age plateau of 2.3 Ga, indicating a relatively young impact event. On the other hand, the whole rock sample yielded two partial isochrons >790°C with low ^{40}Ar/^{36}Ar ratios ranging between 1 and 2, much closer to the solar value, and apparent ages close to 3 Ga. This outlines a scenario of a complex impact, degassing, compaction and irradiation history.

Lebedev[1] E. B., Roschina[1] I. A., Kononkova[1] N. N., Zevakin[1] E. A., Averin[2] V. V. Influence of physical-chemical properties on accumulation of the iron-sulfide phases in partial molten silicate melt

[1]V. I. Vernadsky Institute of Geochemistry and Analytical Chemistry RAS, Moscow leb@geokhi.ru

[2]A. A. Baykov Institute of metallurgy and material science RAS, Moscow

The modeling is carried out on a high-temperature centrifuge at temperatures 1440–1460°C and in the controlled conditions of oxygen potential, with a high degree of extraction of iron from silicate melt. Calculations of the values of oxygen fugacity were also performed on the basis of chemical composition of the phases of the quenched samples after the experiments, using the empirical relationship and also on the program of Terra.

Key words:[experimental study, magmatic melts, metallic phases, accumulation, segregation, oxygen fugacity, calculations.]

Reference: Lebedev, E. B., I. A. Roschina, N. N. Kononkova, E. A. Zevakin, V. V Averin (2012), Influence of physico-chemical properties on accumulation of the iron-sulfide phases in partial molten silicate melt, *Vestnik ONZ RAN. 4*

As expected that on the early stages of the evolution of planetary bodies differentiation processes of magmatic melts, accumulation and segregation of metallic phases and the separation of siderophile elements occur at high temperatures and low oxygen fugacity, at several orders of magnitude lower than the iron-wustite buffer (IW), $\Delta\log f\text{O}_2$ (IW), = ~ -(4.5–5.5). The processes of magmatic differentiation have complex dynamics. During experimental study of the possible mechanisms of formation of metallic cores of planetary bodies (Moon) the greatest difficulties arise in the accumulation of metallic phases from partially molten model planetary matter, especially when the maximum extraction of small amounts of the metallic phases [*Lebedev, Galimov, 2012*]. Modeling is carried out on high-temperature centrifuge at 1440–1460°C and controlled oxygen potential. When a high degree of extraction of iron (up to 0.16% FeO) of the olivine silicate melt can become almost forsterite, silicate phase becomes almost non ferriferous melt. This indicates to the fact that the chemical composition of the products of the experiment corresponds to a high reduction of phases. Calculations Kadik A.A. also show high reduction conditions [*Kadik, 2008*].

Calculations of the values of oxygen fugacity (fO_2, fig. 1) were also performed on the basis of chemical composition of the phases of the quenched samples after the experiments, using the empirical relationship [*Ariskin et al., 1992*]. $\lg fO2 = -22446{,}53 / T + 1{,}948 [\lg (X_{FeO}) - s]$, where: s-is the regression parameters, Xi components of silicate melt in the form of oxides (mol%). The obtained value of oxygen fugacity $\Delta \log fO_2$ (IW) = - (5.8 ± 0.3) correspond to 0.16% FeO.

A diagram of the concentrations of P_{fO2}(atm)–T for the initial composition: (SiO_2 - 57.81) + (MgO – 16.59) + (FeO – 0.16) + (Al_2O_3 – 11.71) + (CaO – 7.37) + (TiO_2 – 0.38) + (ZrO_2 – 3.79) + (C –– 0.3) + (S – 0.65) + (P – 0.2).

The basis of the method used by the program "Terra" [*Trusov, 2002*] is the principle of maximum entropy, which is valid in accordance with the second law of thermodynamics for any system equilibrium, regardless of the way in which the system has reached equilibrium.

The program allows to display of the concentration of the reaction products in different scales: in the mass fraction (mol%), in the partial pressure of the reaction in M-Pas or atm.

Both methods of calculation of oxygen fugacity for the experimental data show similar values.

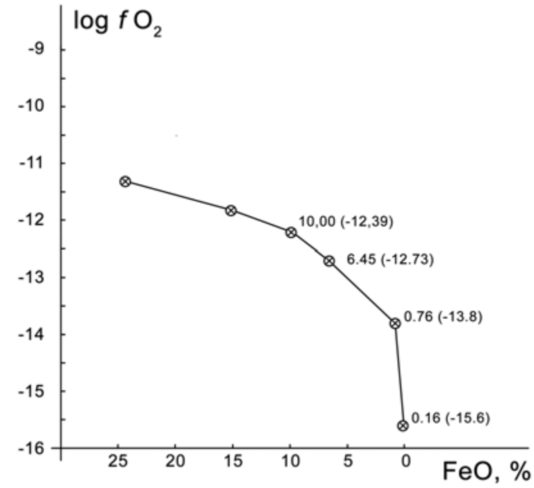

Fig. 1. The dependence of oxygen fugacity, in depending from the iron content in the melt, T=1440°C

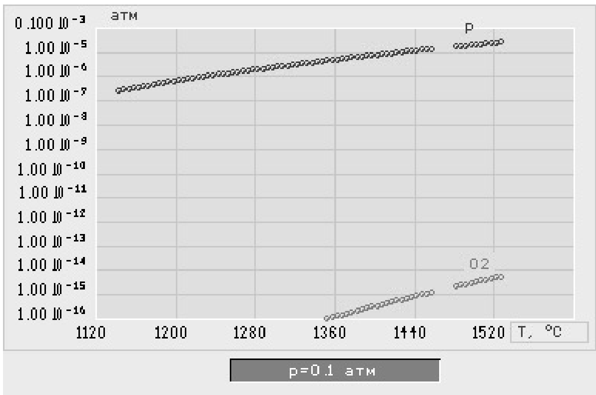

Fig. 2. The dependence of oxygen fugacity in model the melt

This work was supported by RFBR Grant 07-05-00630 and Grant Program of the Presidium of RAS № 24.

References:

1. Averin, V. V. (2007). The thermodynamic modeling of the interaction of hydrogen with oxides of titanium, Metal Technology, №3, pp. 40–43.
2. Ariskin, A. A., A. A. Borisov, G. S. Barmina. (1992). Modeling of the equilibrium iron - silicate melt in basaltic systems, Geochemistry, No 9, pp.1231–1240.
3. Кадик, A. A. (2008). Degassing of the Earth's mantle during melting and forming of metal core of the planet: the results of experimental modeling, The problem of the origin and evolution of the biosphere, Ed. E. M. Galimov, M.: Book house "LIBROKOM", pp. 367–379.
4. Lebedev, E. B., E. M. Galimov. (2012). Experimental simulation of the formation of the metallic core of the Moon in terms of partial melting, Geochemistry, No 8. pp.1–12.
5. Trusov, B. G. (2002). Programme system Terra for simulations of phase and chemical equilibria in plasma-chemical processes, Proceedings of the 111 international Symposium on theor. and appl. Plasma chemistry, Ivanovo, pp. 217–220.

Lyul A.Yu. On secondary element fractionation in the metal from Norton County aubrite

V. I. Vernadsky Institute of Geochemistry and Analytical Chemistry RAS, Moscow ajull@mail.ru

The influence of a secondary element fractionation on the Fe,Ni-phase composition of enstatite achondrites is considered on the basis of trace element concentrations in the nodules and fine-grained metal from Norton County aubrite. It is shown that the primary metal composition of Norton County has been greatly changed by secondary processes on the aubrite parent body such as thermal metamorphism and partial melting of an initial metal.

Key words: [Norton County aubrite, Fe,Ni-phase, element fractionation, secondary processes]

Reference: Lyul, A. Yu (2012), On secondary element fractionation in the metal from Norton County aubrite, *Vestnik ONZ RAS,4*, (doi: ………)

Ustinova G. K. Meteoritic nanodiamonds and primary cosmic rays

Vernadsky Institute of Geochemistry and Analytical Chemistry, RAS, Moscow ustinova@dubna.net.ru

Isotopic anomalies of xenon in the nanodiamonds of chondrites testify to the rigid radiation and magneto hydrodynamic conditions at the last supernova explosion prior to formation of the Solar system.

Key words: [cosmic rays, astrophysical sources, shock waves, diffusive acceleration, meteoritic nanodiamonds, isotopic anomalies]

Citation: Ustinova, G. K. (2012), Meteoritic nanodiamonds and primary cosmic rays, *Vestnik ONZ RAN, 4,*

Problems of origin of cosmic rays

The origin of cosmic rays is one of the key present-day problems. Potential sources of cosmic rays can be both in the Galaxy (e.g., supernova outbursts, pulsars, explosions in the nucleus of the Galaxy), and in the Metagalaxy (e.g., close superclusters of galaxies, quasars) [*Berezinskii et al., 1990*]. Numerous models considering different astrophysical objects, combinations of them, and accompanying processes as possible sources of cosmic rays are developed. An adequacy criterion of models is their ability to reproduce the observed spectrum and composition of primary cosmic rays (PCRs), the energy range of which extends up to ~10^{21} eV to date [*Haungs, 2009*]. Characteristic features of the PCR spectrum are changes of the spectral index, i.e., kinks of the spectrum at ~10^{15}–10^{17} eV, at ~10^{16}–10^{18} eV, and at the highest energies ≥10^{19} eV, as well as the gradual enrichment of the spectrum with heavy ions: above 10^{17} eV the spectrum consists almost entirely of iron. There are two approaches to the interpretation of experimental data: nuclear physical and astrophysical. In the nuclear physical interpretation, observed features of the PCR spectrum are connected with the possible formation of new particles, new interactions, or new states of matter (e.g., quark-gluon plasma) at energies ≥10^{15} eV, which could influence the spectrum character and PCR composition. However, recent experiments at the Large Hadron Collider (LHC) at the energy of the incident particle ≥10^{16} eV did not show any deviations from the standard model of particles and interactions [*LHC News, 2010*], so this fact allows giving preference to the astrophysical aspect.

Universal mechanism of cosmic ray acceleration: The main sources of PCR in our Galaxy are supernova outbursts [*Berezinskii et al., 1990*]. A reliable justification of this hypothesis was the discovery of the universal mechanism of cosmic ray acceleration in shock waves accompanying supernova outbursts [*Berezhko, Krymsky, 1988*]. While the ejected matter of the supernova moves in the turbulent interstellar medium, a shock wave forms; it represents a magneto-hydrodynamic discontinuity, at the front of which in the matter compression region, the regular magnetic field undergoes a jump, and in addition, the stochastic magnetic field of the plasma turbulence develops; this creates scattering centers for the diffusive scattering of charged particles. The physical meaning of the acceleration mechanism is the following: as a result of the diffusive scattering, charged particles can repeatedly cross the compression region at the wave front, getting an energy increment in generated inductive electric fields; i.e., the longer particles are held in the wave front region, the more they are accelerated. In other words, the larger the particle velocity and, therefore, its path before the scattering, the more often and from larger distances the particle can return to the front region and get the velocity increment. As a result, the particle power-law energy spectrum forms: $F(E) \sim E^{-\gamma}$ with the index $\gamma = (\sigma + 2)/(\sigma - 1)$, where σ is the degree of matter compression at the shock front [*Berezhko, Krymsky, 1988*]. Obviously, in strong shock waves (at $\sigma >> 1$), a very hard spectrum of accelerated particles (with $\gamma \rightarrow 1$) can be formed. Similarly, heavy ions with a large path will have a priority of acceleration; this leads to the enrichment of the spectrum with heavy ions proportionate to A/Z, where A is the mass number and Z is the ion charge.

In fact, the process of the diffusive acceleration of particles by shock waves is the knocking-out of new particles from the background plasma by the shock wave and the transferring of particles from the low-energy region of the spectrum to its high-energy part. This leads to the increase of fluxes of nuclear-active particles above the threshold energy of nuclear reactions and, accordingly, to the increase of the rate of isotope production in spallation reactions (see [*Ustinova, 2007*] and references therein). In addition, the change of the energy spectrum of nuclear-active particles leads to the change of the weighted spectrum-averaged cross sections for the production of many isotopes, excitation functions of which are sensitive to the particle spectrum shape. As a result, in reservoirs reprocessed by shock waves, for example, in expanding shells of supernovas, absolutely different isotopic and elemental ratios than those in matter not affected by such reprocessing are formed. Indeed, in samples of extraterrestrial matter, numerous isotopic anomalies that could have been caused by such violations of isotopic ratios are observed [*Ustinova, 2002; 2007; 2011a*].

Isotopic anomalies of xenon in relic nanodiamond grains, identified in carbonaceous and nonequilibrium ordinary chondrites [*Huss, Lewis, 1995*], are of particular interest. For meteoritic nanodiamonds, a bimodal character of xenon release is observed: mainly as the Xe-P_3 component with the almost-solar isotopic composition and as the anomalous Xe-*HL* component with the exotic isotopic composition (enriched about twice with light ^{124}Xe, ^{126}Xe isotopes and heavy ^{134}Xe, ^{136}Xe isotopes). Besides the processes of nucleosynthesis, all xenon isotopes could be produced in reactions of spallation of neighboring Ba, Cs, Ce, and La nuclei by high-energy particles [*Ustinova, 2007; 2011a*]. The anomalous Xe-HL in meteoritic nanodiamonds was formed simultaneously with nanodiamonds themselves during the shock wave propagation at the last supernova explosion before the formation of the Solar System [*Ustinova, 2011a*]. Indeed, since the conversion of the protosolar nebula into the protostar was accompanied by huge changes in the physical state of the matter, all of the previously synthesized nanodiamond grains, even if preserved, should have lost all their noble gases. But the last supernova was not the SnII [*Ustinova, 2007*]. The absence of excesses of heavy extinct radionuclides (products of the *r*-process) in CAI of carbonaceous chondrites with a formation interval of ~1 million years indicates that the last supernova during the formation of the Solar System was the carbon-detonation supernova SnIa which was devoid of both a heavy core and a hydrogen shell [*Ustinova, 2007*]. During its explosion, all of the rock-forming elements up to the iron peak are synthesized, but products of the *r*-process are absent. This fact puts spallation reactions in the key role of the generation of isotopes of xenon captured by nanodiamonds.

The modeling of rates of xenon isotope production in spallation reactions of neighboring Ba, Cs, Ce, and La nuclei by high-energy protons with different spectrum hardness (at variations of γ from 1.1 to 6) shows [*Ustinova, 2011a*] (see rows 3 and 6 of the table 1) that the isotopic ratios observed in chondrites in the Xe-*HL* component are higher than the corresponding isotopic ratios in the Xe-P_3 component [*Huss, Lewis, 1995*] almost as much as isotopic ratios of xenon generated under hard radiation conditions of the matter reprocessing by shock waves (γ = 1.1, for example, in expanding shells of supernovas) are higher than those in the matter not affected by such reprocessing (γ = 3, for example, in the main volume of the protosolar cloud). This reveals the spallogenic nature of both anomalous and normal components of xenon and points to the different hardness of the energy spectrum of nuclear-active particles as the major cause of the difference in their isotopic systems.

The table 1 implies that spallation reactions are insufficient only for the generation of the heaviest ^{134}Xe and ^{136}Xe isotopes, and an additional nucleogenetic source is required. However, the most favorable for the synthesis of the nanodiamond front of the explosion shock wave was enriched with these isotopes because of the preferential acceleration of just heavy isotopes of the medium [*Berezhko, Krymsky, 1988*], in particular, of products of the *r*-process from previous explosions of SnII, at the shock front. Thus, during the nanodiamond synthesis in the shock wave from the SnIa explosion, the xenon produced in spallation reactions by protons which were accelerated by the shock wave was captured, and heavy isotopes of xenon from preceding explosions of supernovas, with which the wave front was enriched, were captured. This is what formed the anomalous Xe-*HL* component. The Xe-P_3, could be captured simultaneously, but most likely, this component was implanted later during the uniform mixing of the matter of the supernova and the protosolar cloud by supersonic turbulence.

The table 1 also allows comparing the observed isotopic ratios of the xenon in the Xe-*HL* component with theoretical ones at $\gamma = 1.1$ (row 7) and the observed isotopic ratios of the xenon in the Xe-P_3 component with theoretical ones at $\gamma = 3$ (row 8). It is seen well that the xenon preserved in the nanodiamond is significantly heavier than the originally generated xenon, and almost to the same extent for both components. The latter suggests that processes that led to such weighting occurred after the formation of these components, most likely, during the accretion. Indeed, the multiple acts of partial recrystallization of nanodiamond grains at the stage of the young Sun were accompanied by the diffusion and escaping of xenon from destroyed traps, cracks, and other disturbances of the crystal lattice and, consequently, led to the gradual enrichment of the isotopic system of the preserved xenon with heavy isotopes in comparison with its original isotopic system during the generation.

Table 1. Isotopic ratios of Xe in the observed Xe-*HL* ^{a} and Xe-P_3 ^{a} components in nanodiamonds of chondrites and the similar ratios, generated by the shock wave accelerated nuclear-active particles with various hardness of the energy spectrum $F(>E_0)\sim E^{-\gamma}$: at $\gamma = 1.1$ and $\gamma = 3$

N	Xe components	$\frac{^{124}Xe}{^{132}Xe}$	$\frac{^{126}Xe}{^{132}Xe}$	$\frac{^{128}Xe}{^{132}Xe}$	$\frac{^{129}Xe}{^{132}Xe}$	$\frac{^{130}Xe}{^{132}Xe}$	$\frac{^{131}Xe}{^{132}Xe}$	$\frac{^{134}Xe}{^{132}Xe}$	$\frac{^{136}Xe}{^{132}Xe}$
1	$Xe\text{-}HL^{\,a}$	0.0084	0.0057	0.091	1.06	0.154	0.844	0.636	0.7
2	$Xe\text{-}P_3^{\,a}$	0.0045	0.004	0.081	1.04	0.159	0.823	0.377	0.31
3	$\frac{Xe-HL^{\,a}}{Xe-P_3^{\,a}}$	**1.86**	**1.43**	**1.12**	**1.02**	**0.97**	**1.03**	**1.85**	**2.26**
4	$Xe\ (\gamma\sim 1)$	0.58	1.38	3.16	4.16	1.29	9.61	0.036	0.0065
5	$Xe\ (\gamma = 3)$	0.31	0.90	2.69	4.44	1.18	10.44	0.026	0.0045
6	$\frac{Xe\ (\gamma\sim 1)}{Xe\ (\gamma = 3)}$	**1.87**	**1.53**	**1.17**	**0.94**	**1.09**	**0.92**	**1.38**	**1.44**
7	$\frac{Xe\ (\gamma\sim 1)}{Xe-HL^{\,a}}$	69.05	242.11	34.73	3.92	8.38	11.39	0.057	0.0093
8	$\frac{Xe\ (\gamma=3)}{Xe-P_3^{\,a}}$	68.89	225.00	33.21	4.27	7.42	12.69	0.069	0.0145

[a] According to data from [*Huss, Lewis, 1995*].

Magneto hydrodynamic conditions in the early Solar system: The obtained results demonstrate the quantitative estimations of isotope anomalies in the primordial matter due to the diffusive acceleration of cosmic rays by shock waves; these estimations represent a subtle tool for studying processes in the early Solar System [*Ustinova, 2011a*]. The magneto hydrodynamic conditions of particle acceleration at the stage of the free expansion of the shock wave during the SnIa explosion are concretized for the first time. The experimental evidence for the formation of the power law spectrum of particles with the index $\gamma = 1.1$ indicates that the degree of matter compression at the front of the explosion shock wave from the SnIa explosion was $\sigma = 31$, which corresponds to the Mach number $M \sim 97$ at $\sigma \sim M^{3/4}$ [*Ustinova, 2011b*]. This implies that the interstellar magnetic field ($B \sim 10^{-5}$ G), which is proportionate to the degree of compression, increased by a factor of 31 at the shock wave front, and the maximum energy of accelerated particles, which is proportionate to the magnetic field, increased by the same factor. Since the mean interstellar magnetic field is sufficient to accelerate protons to $\sim 10^{14}$ eV [*Berezinskii et al., 1990*], the energies of $\sim 3 \cdot 10^{15}$ eV were reached at the acceleration by the explosion shock wave. Further investigations should show how these energies were modified during the further evolution of the shock wave in accompanying processes, what fraction they contributed to the total PCR spectrum from different sources, and for what part of the spectrum they turned out to be the most operative. Indeed, the effects of high radiation conditions are observed in the extinct radionuclides in some refractory grains of the Ca and Al rich inclusions (CAI) of carbonaceous chondrites (see Figs. 1 and 2 for ^{26}Al and ^{53}Mn, respectively), as well as they follow from the abundances of isotopes of the light elements Li, Be and B (Fig.3) [*Ustinova, 2002*]. Since the interval of CAI formation is ~ 1 My [*Srinivasan et al, 1996*], the stage of free expansion of explosive shock wave was long enough and should make noticeable contribution to the formation of the highest energy part of integral spectrum of the primary cosmic rays.

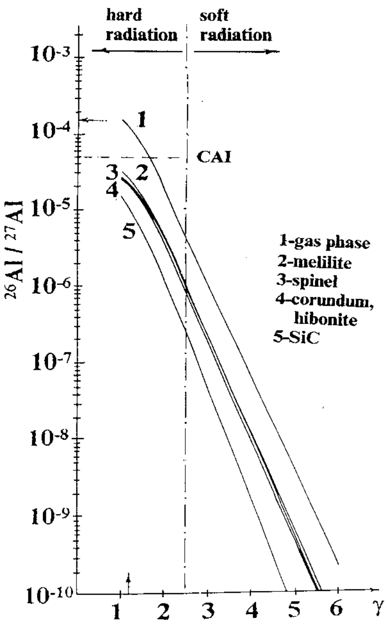

Fig. 1 The observed range of $^{26}Al/^{27}Al$ in CAI of carbonaceous chondrites reaches ~10^{-3} (while the canonic value, marked by the dashed line, is $5 \cdot 10^{-5}$), which corresponds to γ ~1.

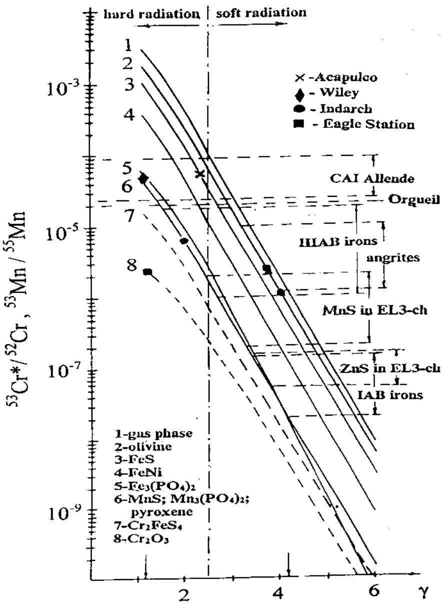

Fig. 2 In CAI of the Allende carbonaceous chondrite, as well as, in some differentiated meteorites, the minerals with the $^{53}Mn/^{55}Mn$ relation, formed in spallation reactions at γ ~1 are observed.

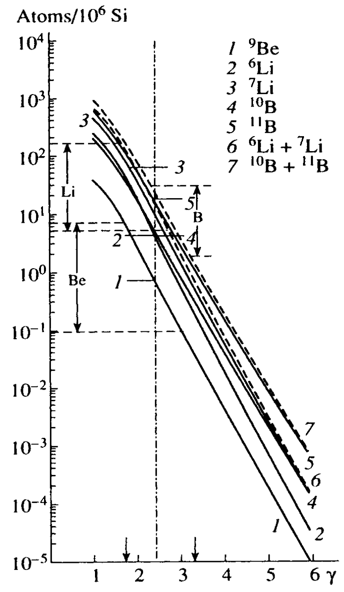

Fig. 3 The measured range of abundances of Li, Be and B isotopes, in particular, ^7Li, could be produced in spallation reactions with the shock wave accelerated particles if γ ~1.

This work is supported in part by the Program No. 22 of Fundamental Research of Russian Academy of Sciences.

References:

1. Berezinskii, V. S., S. V.Bulanov, V. A. Dogiel', V. L. Ginzburg, and V. S. Ptuskin (1990). *Astrophysics of Cosmic Rays;* Elsevier: Amsterdam.
2. Berezhko, E. G., and G. F. Krymsky (1988). Acceleration of cosmic rays by shock waves. *Sov. Phys. Usp. 31*, pp. 27–51.
3. Haungs, A. (2009). *High-light talk 31st ICRC* Lodz. http://icrc2009.uni.lodz.pl/dl.php?fname=haungs.pdf
4. Huss, G. R., and R. S. Lewis (1995). Presolar diamond, SiC, and graphite in primitive chondrites: Abundances as a function of meteorite class and petrologic type. *GCA 59*, pp. 115–160.
5. LHC News (2010). http://elementy.ru/LHC/news
6. Srinivasan, G., S. Sahupal, A. A. Ulyanov, and J. N. Goswami (1996). Ion microprobe studies of Efremovka CAIs: II. Potassium isotope composition and ^{41}Ca in the early Solar system. *GCA* 60, pp. 1823–1835.
7. Ustinova, G. K. (2002). Mechanisms of Isotopic Heterogeneity Generation by Shock Waves in the Primary Matter of the Solar System, *Geochem. Intern., 40*, pp. 915–932.
8. Ustinova, G. K. (2007). On the problem of the Solar system origin: The regularities of noble gas fractionation in shock waves. *Sol. System Res. 41*, pp. 231–255.
9. Ustinova, G. K. (2011a). Production of anomalous Xe in nanodiamond in chondrites during the last supernova explosion predating the origin of the Solar system. *Geochem. Intern., 49,* pp. 555–567.
10. Ustinova, G. K. (2011b). Effects of the diffusive acceleration of particles by shock waves in the primordial matter of the Solar system. *Doklady Physics 56,* pp. 219–223.

Tselmovich V. A. Possible microscopic traces of the Tunguska meteorite

Geophysical Observatory "Borok" IPE RAS tselm@mail.ru

The author studied the branch, found in a small funnel in the peat bog on the northern islands of the southern marshes on the site of the Tunguska phenomenon. By X-ray microanalysis and cathodoluminescence was studied in a branch, found in the peat bog on the northern islands of the southern marshes on the site of the Tunguska phenomenon. It found trace minerals, the origin of which can usually be both space and terrigenous

Key words: [Tunguska meteorite, native metals, diamond, moissanite, cathodoluminescence.]

Citation: Tselmovich, V. A. (2012). Possible microscopic traces of the Tunguska meteorite. *Vestn. Otd. nauk Zemle, 4,*

A key element in studying the nature of the Tunguska meteorite is the question of how it was material (elemental and isotopic) composition. Starting with the expedition, LA Kulik, finding the substance of the Tunguska meteorite was occupied for several generations of researchers. The results of these long-term efforts are reflected in the numerous reviews and original publications. However, today it can be argued that the cosmic matter, which could be guaranteed to be identified with the substance of the Tunguska meteorite has yet been found. The substance of the hypothetical Tunguska meteorite was found in any significant numbers, but were found microscopic silicate and magnetite pellets, as well as an increased content of some elements, indicating a possible origin of cosmic matter. Thus, the Italian researchers analyzed the particles found in the resin in 1908 [*Longo et al., 2003; Serra et. al., 1994*], were found to differ from the particles of the earlier and later. The resin on the roots of a fallen tree they saw as "retarded trap", since the substance of the meteorite has been falling after the explosion, and the roots were gradually from the ground, and then they separated resin. The resulting samples were studied in the University of Bologna with an electron microscope. A distinguishing feature of most predominant particles found in the resin in 1908 was their shape with smooth edges, sometimes spherical, indicating a strong thermal effects. The particles found in the resin before and after 1908, usually have pointed edges, or "fluffy" appearance that is characteristic of many background particles are always present in the air (dust, cosmic, volcanic, biological or industrial origin). The observed difference led to the conclusion that most of the particles belonging to 1908, came to the resin directly from the blown up space body, they could not be raised by the blast from the ground, because then no time to warm up to the melting point.

Thus, the Italians had shown promising analysis of particles trapped in the resin or other parts of the tree to identify the substance of the Tunguska meteorite. However, their results must be supplemented by modern methods of research that was done.

The author studied the branch, found in a small funnel by E.V.Dmitriev in the peat bog on the northern islands of the southern marshes on the site of the Tunguska phenomenon. Initially the discovery was a small sprig of 5 cm long, 2 mm in diameter. Sprig was very similar to a charred. However, she had a polished surface, differed from other similar entities. She did not leave a trace on the paper. Color of branches, even in thin sections, was completely black. On the assumption that the particles of meteoric matter in the explosion penetrated into the wood, the particles were collected from the surface layer of twigs. They were transferred to double-sided carbon tape. Analyzed the chemical composition of microparticles using a energodispersive spectrometer Drycool Oxford Instruments, and then carried out cathodoluminescence study of luminous particles in the spectrometer Mono CL3 firm Gatan. The chemical composition of the most interesting particles, identified by the review cathodoluminescent shooting, was studied after the shooting. A similar technique was previously used in the study of samples from the Cretaceous-Paleogene boundary (Gams, Austria, Stevens Klint, Denmark [*Grachev et. .al., 2009; Korchagin et. al., 2011*]).

As a result, the particles were detected minerals which can have both outer and terrigenous origin. By cosmic particles may include findings of grains that could be generated by strongly reducing conditions. These include particle: native Sn (Fig. 1), Zn (Fig. 2, Fig.6), W (Fig. 3), Cr (Fig. 4), Ni, Al, Fe (Fig. 5). Perhaps the presence of metal carbides. Among these findings highlights the diamond particles (Fig. 8) and moissanite (Fig. 3, Fig. 6). These findings are the best markers of impact events. Similar findings were made in the study of Cretaceous-Paleogene boundary, which is also assumed to impact [*Grachev et. .al., 2009; Korchagin et. al., 2011*]. High-carbon spheroids are shown in Fig. 7. The same was found previously in the boundary sediments in the Permian-Triassic Nedubrovo [*Korchagin et. al., 2010*]. Fine particles of diamond (3x3 mm) and moissanite (2x3 mm) were found by using cathodoluminescence spectrometer. City cathodoluminescence image is shown in Fig. 9. Cathodoluminescence spectra of diamond and moissanite are shown in Fig. 10, 11. The obtained grain diamond is one of the faces of titanomagnetite telluric origin. Apparently, in the process of shock-thermal effects of the fall of the Tunguska meteorite was epitaxial growth of diamond on the brink of titanomagnetite. Both minerals may have a similar crystalline structure. A similar phenomenon - the growth of cosmic matter in the earth with impact - before there was the author of the study astrobleme Tsenher (Mongolia). It was found fusing native iron in the magnetite particle [*Saltykovsky et. al., 2011*].

For telluric minerals include magnetite particles findings, titanomagnetite, iron sulfides, pyroxenes, muscovite, amphibole, quartz, aluminum silicates of different composition. The origin of olivine and iron sulfides may be ambivalent. Of special note finds organic matter whose identity microprobe method is difficult or impossible. Thus, grains of native Al and W are carbon particles containing Al and W in the form of impurity, but rather – in the form of nanoparticles whose size is much smaller than the physical features of X-ray method.

Conclusion. A set of minerals of cosmic origin can be attributed to the discovery E.V.Dmitriev 1908, the fall of the Tunguska meteorite. Clear value for further research of wood disastrous period for the detection of minerals - markers of cosmic matter.

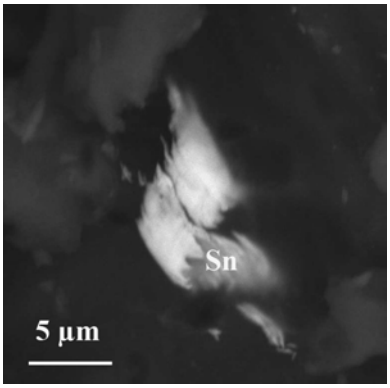

Fig. 1. A particle of native Sn

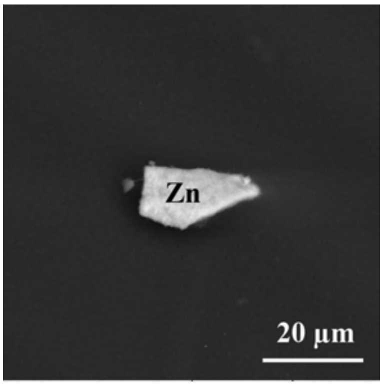

Fig. 2. A particle of native Zn

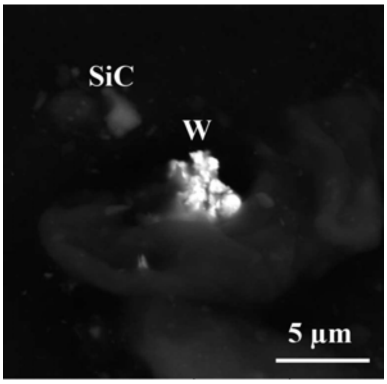

Fig. 3. A particle of native W and SiC moissanite

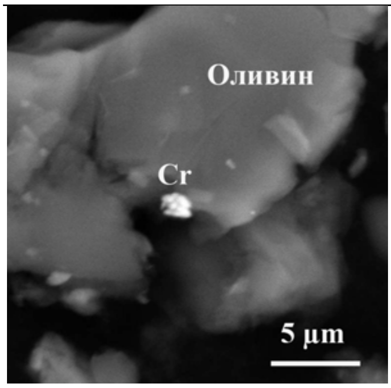

Fig. 4. A particle of native Cr on olivine

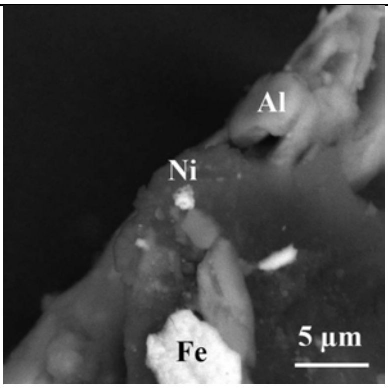

Fig.5. Particles of native Ni, Al, Fe

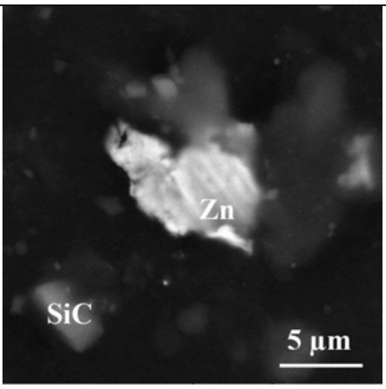

Fig.6. Particles of native W and SiC moissanite

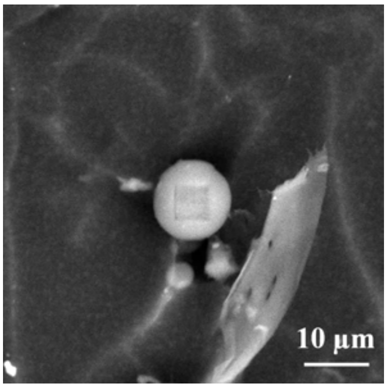

Fig. 7. The organic microspheres

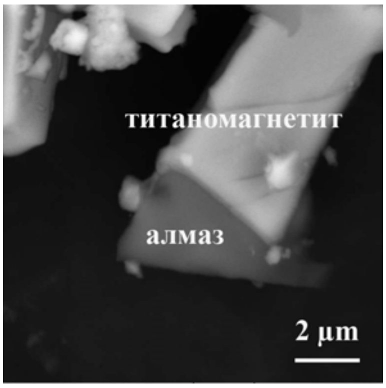

Fig, 8. Diamond in the titanomagnetite, BSE detector

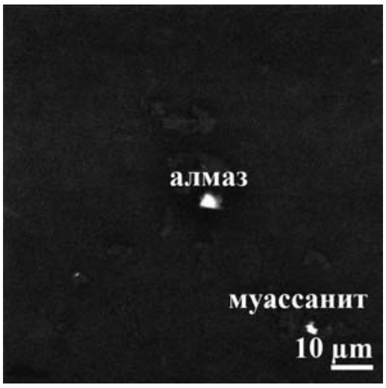

Fig. 9. Cathodoluminescence glow-diamond and moissanite

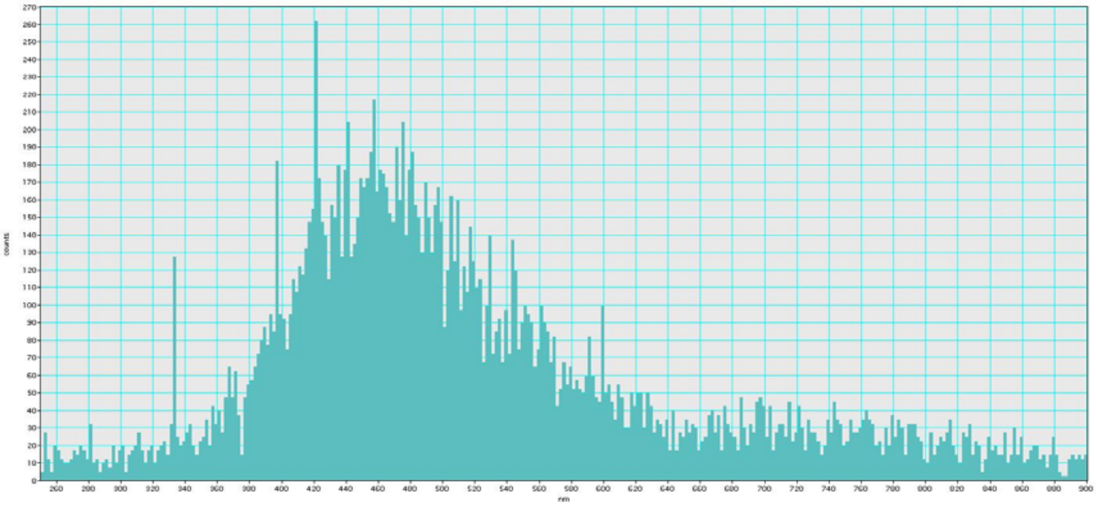

Fig, 10. Cathodoluminescence spectrum of diamond grains (blue glow)

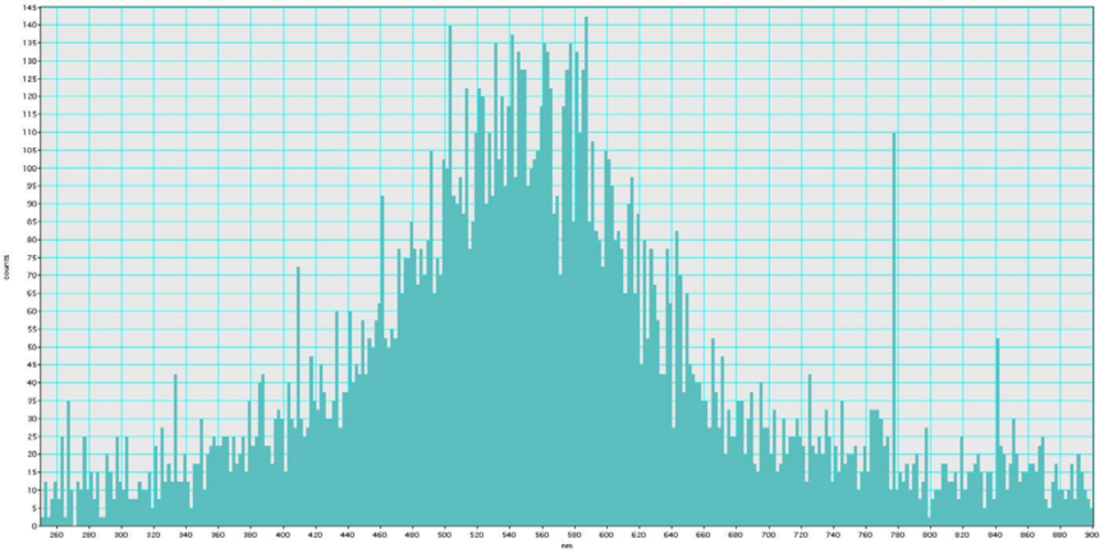

Fig. 11. Cathodoluminescence spectrum of moissanite grains (orange glow)

This work was supported by RFBR, grant 10-05-0017a.

References:

1. Grachev, A. F., Ed. (2009). The K/T Boundary of Gams (Eastern Alps, Austria) and the Nature of Terminal Cretaceous Mass Extinction., doi: 10.2205/2009-GAMSbook, Print companion published by the Geological Survey of Austria, Abhandlungen, 63, 199 pp.
2. Korchagin, O. A., V. A. Tselmovich (2011). Cosmic particles (micrometeorites) and nanospheres from the boundary layer between the chalk and clay Paleogene (K/T) cut Stevens Klint, Denmark, *Doklady RAS*, v. 437, № 4, p. 520–525.
3. Korchagin, O. A., V. A. Tselmovich, V. R. Lozovsky (2010). High-carbon microspheres and spheroids of the boundary deposits of the Permian-Triassic Nedubrovo, Central Russia, *Eleventh International Conference "Physico-chemical and petrophysical studies in the geosciences." Moscow, 11–13, Borok, October 14, 2010 Proceedings,* Moscow, p. 140–142.
4. Longo, C, V. Serra, S. Cecchini, M. Galli (1994). Search for Microremnants of the Tunguska Cosmic Body, *Planetary and Space Science*, v. 42, N 2, p. 163–177.
5. Saltykovsky, A. J., V. A. Tselmovich, T. Bayaraa, A. N. Nikitin, T. I. Ivankina, J. Komatsu, Yu. Ormoo (2011). Impact craters and composition of cosmic matter in the Early Paleozoic structural zone of southern Mongolia, *Twelfth International Conference "Physico-chemical and petrophysical research in earth sciences." Moscow, 3–5, Borok, October 6, 2011 Proceedings*, Moscow, p. 273–277.
6. Serra, R., S. Cecchini, M. Galli, G. Longo (1994). Experimental Hints on the Fragmentation of the Tunguska Cosmic Body, *Planetary and Space Science*, v. 42, N 9, p. 777–783.
7. Tselmovich, V. A. (2012). On the meteoritic origin of native metals in sedimentary rocks, *Diagnostics products in volcanic sediments: Proceedings of Russian conference with international participation, Syktyvkar: IG Komi Science Centre,* p. 190–193.

Shornikov S.I. A thermodynamic study of regularities in vapor composition over oxide compounds (the CaO–MgO–Al_2O_3–FeO–SiO_2 system)

Vernadsky Institute of Geochemistry and Analytical Chemistry RAS, Moscow *sergey.shornikov@gmail.com*

On the basis of the experimental data obtained by the Knudsen effusion mass spectrometry method, we have considered dissociation regularities of complex gaseous oxides contained in the gas phase over the CaO–MgO–Al_2O_3–FeO–SiO_2 system compounds. The thermodynamic calculations took into account the effect of redox conditions on the compounds' evaporation and possible changes in the composition of the condensed phase at evaporation.

Key words: [thermodynamics of evaporation, the CaO–MgO–Al_2O_3–FeO–SiO_2 system, gaseous oxides]

Citation: Shornikov, S. I. (2012), A thermodynamic study of regularities in vapor composition over oxide compounds (the CaO–MgO–Al_2O_3–FeO–SiO_2 system), *Vestnik ONZ RAS, 4, (doi:).*

Studies of substances' high-temperature evaporation are of topical importance for both understanding geochemical and cosmochemical phenomena, and their practical application in various fields of engineering. They acquire special importance in studies into the origin and composition of meteorites, in particular, the substance of CAI white inclusions formed mostly by the CaO–MgO–Al_2O_3–FeO–SiO_2 system compounds.

The goal of this work was to consider evaporation regularities of the CaO–MgO–Al_2O_3–FeO–SiO_2 system compounds related to presence of complex gaseous oxides in the gas phase over them.

As known [*Semenov et al.*, 1976], in the gas phase over oxide compounds there can be both *simple* gaseous oxides consisting of a single element with oxygen compound (X_iO_j), and *complex* gaseous oxides ($X_iY_jO_k$) formed in accordance with the following reactions:

$$[XO_i] = (XO_{i-k}) + k\,(O) \qquad (1)$$

$$[XO_i] = (XO_i) \qquad (2)$$

$$[X_iY_jZ_kO_l] = (X_iY_jZ_kO_l) \qquad (3)$$

$$(X_iY_{j-m}O_{l-p}) + (Y_mZ_kO_p) = (X_iY_jZ_kO_l) \qquad (4)$$

$$(X_iO_{k-m}) + (Y_jO_m) = (X_iY_jO_k), \qquad (5)$$

where X and Y are elements, round brackets designate the gas phase, and square brackets – condensed phase. Their content in the gas phase is usually insignificant. However cases are known where the gas phase above an oxide compound consisted mostly of complex gaseous oxides.

In case of the CaO–MgO–Al_2O_3–FeO–SiO_2 system compounds, as follows from the experimental data obtained by the Knudsen effusion mass spectrometry method, in the 1500–2500 K temperature range in the gas phase above these melts the following complex gaseous oxides were detected: (CaAlO), (CaSiO), ($CaSiO_3$), (MgAlO), (AlSiO) [*Shornikov*, 2003]. Their quantity in the gas phase is inappreciable and does not exceed 1 % in the total concentration, the predominant gas phase components being atomic and monoxide gaseous compounds – (Ca), (Mg), (Al), (AlO), (Fe), (FeO), (SiO).

Let us consider the evaporation regularities of the CaO–MgO–Al_2O_3–FeO–SiO_2 system compounds from the viewpoint of changes in the content of these complex gaseous oxides in the gas phase above oxide compounds depending on 1) condensed phase composition, 2) temperature and 3) redox conditions of evaporation of compounds in this multicomponent system.

Fig. 1 shows the vapor species partial pressures of the gas phase $p\,(i)$ and changes in the of the gas phase composition $x\,(i)$ over the alumosilicate melt depending on the condensed phase composition $x\,(SiO_2)$ at 2200 K. As follows from Fig. 1, the complex gaseous oxide (AlSiO) quantity in the gas phase increases as the silicon dioxide [SiO_2] content in the condensed phase decreases.

The observed increase in the (AlSiO) content in the gas phase over the melt follows from the expression conditioned by equilibrium (5):

$$p(X_iY_jO_k) = \frac{p(X_iO_{k-m})\,p(Y_jO_m)}{K_{r5}}\ , \qquad (6)$$

which in this case can be written as:

$$p(\mathrm{AlSiO}) = \frac{p(\mathrm{Al})\,p(\mathrm{SiO})}{K_r}\ , \qquad (7)$$

where K_r is the reaction equilibrium constant. Calculation of the concentration dependences $p\,(i)$ and $x\,(i)$ was executed, as before, within the framework of the thermodynamic approach developed [*Shornikov*, 2009].

Thus, an increase in the gaseous alumosilicate content in the gas phase is proportional to the p (Al) and p (SiO) product increase, which corresponds, in its turn, to reduction of partial oxygen pressure of according to equilibrium (1).

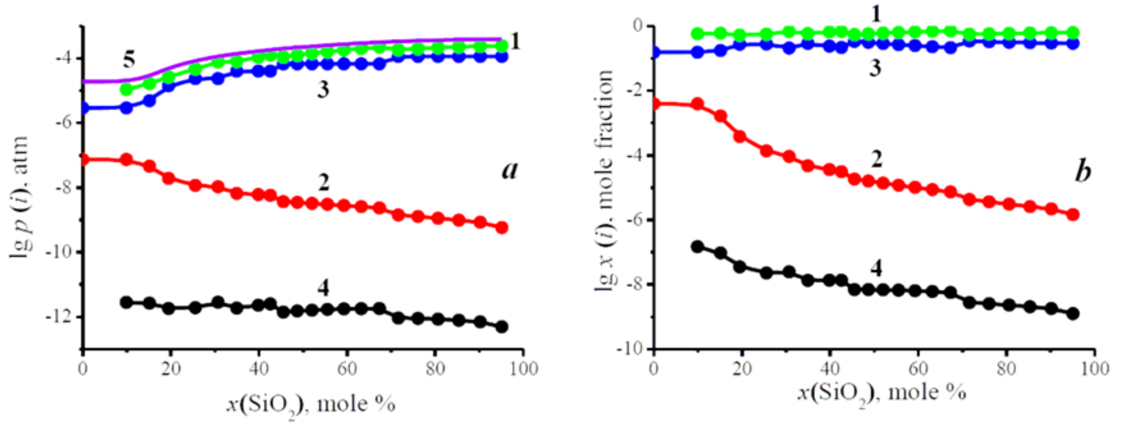

Fig. 1. The calculated dependencies of the vapor species partial pressures (*a*) and the gas phase compositions (*b*) over the Al_2O_3–SiO_2 system melts at 2200 K. The calculations based on the experimental data [*Shornikov*, 2002].
Table of symbols: 1 – (SiO), 2 – (Al), 3 – (O_2), 4 – (AlSiO), 5 – the total vapor pressure over melt.

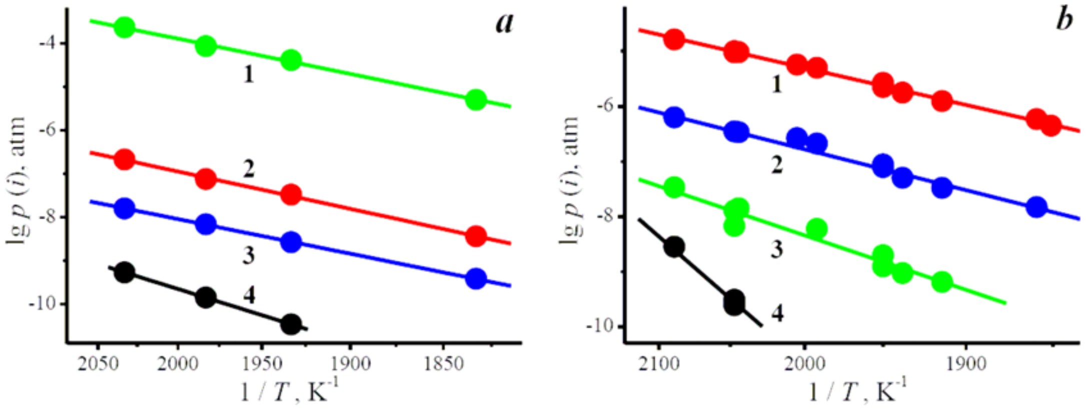

Fig. 2. The experimental temperature partial pressures dependencies of vapor species over oxide compounds:
a – mullite: 1 – (SiO), 2 – (Al), 3 – (O), 4 – (AlSiO);
b – spinel: 1 – (Mg), 2 – (O), 3 – (AlO), 4 – (MgAlO).
The data obtained by the Knudsen effusion mass spectrometric method [*Shornikov*, 2002; *Shornikov*, 2001].

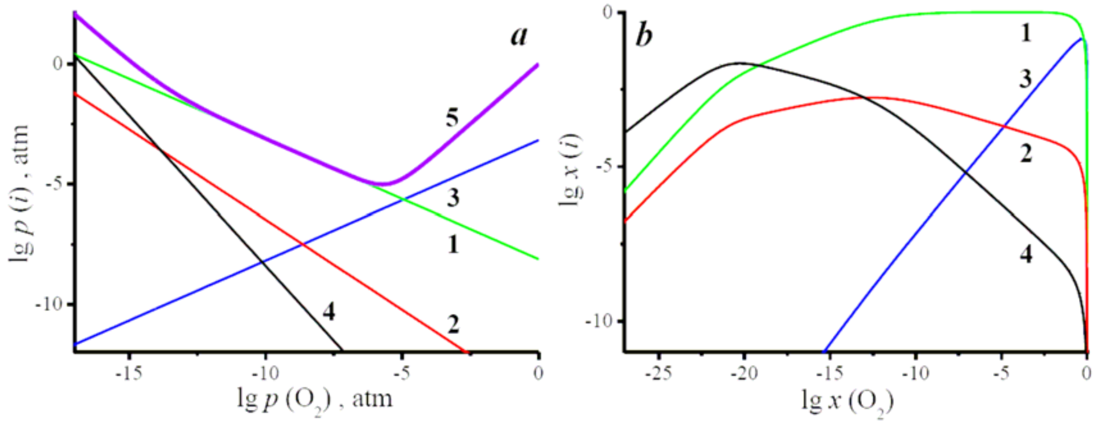

Fig. 3. The calculated partial pressures of vapor species of gas phase over mullite *vs* the molecular oxygen partial pressure (*a*) and the gas phase compositions over mullite (*b*) at 2200 K. The calculations based on the experimental data [*Shornikov*, 2002].
Table of symbols: 1 – (SiO), 2 – (Al), 3 – (O), 4 – (AlSiO), 5 – the total vapor pressure over melt

Typical temperature dependences of the vapor species partial pressures in the gas phase above oxide compounds for mullite $Al_6Si_2O_{13}$ and magnesium spinel $MgAl_2O_4$ are shown in Fig. 2. From Fig. 2 it is seen that the complex gaseous oxides' (AlSiO and MgAlO) content in the gas phase above the oxide compounds increases along with temperature growth in the temperature interval under study in advance of the partial pressure increase of simple gas phase components: (Al) and (SiO) in case of mullite (Fig. 2*a*) and (Mg) and (AlO) in case of spinel (Fig. 2*b*). This increase, like in the case considered above, is apparently caused by equilibrium (5), according to which the complex gaseous oxide partial pressure is proportional to the product of the corresponding partial pressures of simple gas phase components.

The influence of redox conditions during evaporation of the CaO–MgO–Al_2O_3–FeO–SiO_2 system compounds on the complex gaseous oxides' content in the gas phase can be illustrated by Fig. 3. Fig. 3 shows two typical high-temperature dependences for mullite:

1) dependence of the partial pressures of components in the gas phase above the oxide melt on the partial pressure of molecular oxygen (Fig. 3*a*) and

2) dependence of the composition of the gas phase above the oxide depending on the molecular oxygen content in the gas phase (Fig. 3*b*). Both dependences are calculated, as above, within the framework of the thermodynamic approach Calculation of the concentration dependences *p* (*i*) and *x* (*i*) was executed, as before, within the framework of the thermodynamic approach developed and described in details in [*Shornikov*, 2009].

As follows from Fig. 3*a*, the partial pressure of the complex gaseous oxide (AlSiO), as well as partial pressures of simple gas phase components (Al) and (SiO), increase with as the partial pressure of the molecular oxygen over a melt decreases. At the same time, one observes a sharp increase in the content of the gaseous (AlSiO) at a low molecular oxygen content in the gas phase above the melt (Fig. 3*b*). These regularities are probably also conditioned, as well as in case of dependences of the complex gaseous oxides' content in the gas phase above the melts under study, on the condensed phase composition (Fig. 1) and temperatures (Fig. 2), by their dissociation processes, according to equilibriums (1) and (5).

Thus, on the basis of the completed study into the evaporation regularities of the CaO–MgO–Al_2O_3–FeO–SiO_2 system compounds related to the presence of complex gaseous oxides in the gas phase above them, it is possible to draw the following conclusions:

1. For the case of oxide compounds of the system under consideration, the complex gaseous oxides' ($X_iY_jO_k$) content in the gas phase above oxide compounds is low, which is apparently related to their considerable dissociation.
2. The complex gaseous oxides' ($X_iY_jO_k$) content in the gas phase over the oxide compounds under consideration depends on the condensed phase a composition, which conditions the course of dissociation processes.
3. The complex gaseous oxides' ($X_iY_jO_k$) content in the gas phase over the oxide compounds under consideration increases as the temperature grows in accordance with equilibrium in the gas phase (5).
4. The complex gaseous oxides' ($X_iY_jO_k$) content in the gas phase over the oxide compounds under consideration depends on the redox conditions of condensed phase evaporation. Typical for evaporation in reduction environments is a substantial increase in the complex gaseous oxides' ($X_iY_jO_k$) content of in the gas phase above the compounds

The author thanks Igor V. Kaspin (Herzen State Pedagogical University of Russia, Saint-Petersburg) for technical assistance.

References:

1. Semenov, G. A., E. N. Nikolaev, K. E. Frantseva (1976). Mass spectrometry application in inorganic chemistry. Leningrad, Khimiya. 152 pp.
2. Shornikov, S. I. (2001). Vaporization processes and thermodynamic properties of magnesium aluminate, Proc. X Russian conference *Structure and properties of metal and slag melts*. Vol. 3. Experimental investigations of structure and properties of slag melts. Chelyabinsk: SUSU, pp. 73–76.
3. Shornikov, S. I. (2002). Thermodynamic study of the mullite solid solution region in the Al_2O_3–SiO_2 system by mass spectrometric techniques, *Geochem. Int.*, vol. 40, suppl. 1, pp. S46–S60.
4. Shornikov, S. I. (2003). Thermodynamic properties of the melts and vapors of the CaO–MgO–Al_2O_3–SiO_2 system determined by the mass spectrometric study, *Vestnik Otdelenia nauk o Zemle RAN*, vol. 21, No. 1, http://www.scgis.ru/Russian/cp1251/h_dgggms/1–2003/informbul–1/magm–10e.pdf.
5. Shornikov, S. I. (2009). Investigation of abilities of thermodynamic approaches on calculations of oxide activities in the compounds of the CaO–MgO–Al_2O_3–SiO_2 system, *Vestnik Otdelenia nauk o Zemle RAN*, vol. 27, No. 1, http://www.scgis.ru/russian/cp1251/h_dgggms/1–2009/informbul–1_2009/planet–33.pdf.
6. Shornikov, S. I. (2009). A thermodynamic study of evaporation kinetics of the CaO–MgO–Al_2O_3–FeO–SiO_2 system melts, *Vestnik Otdelenia nauk o Zemle RAN*, vol. 27, No. 1, http://www.scgis.ru/russian/cp1251/h_dgggms/1–2009/informbul–1_2009/planet–34.pdf.

Yakovlev [1] O. I., Dikov[2] Yu. P., Gerasimov[3] M. V., Buleev[2] M.I. Silicate cluster vaporization: new experimental data

[1]Vernadsky Institute of Geochemistry and Analytical Chemistry RAS, Moscow yakovlev@geokhi.ru

[2]Institute of Raw Deposits, Petrography, Mineralogy and Geochemistry RAS, Moscow

[3]Space Research Institute RAS, Moscow

The vaporization of silicate minerals may be divided into three types: 1) congruent vaporization with dissociation substances in vapor phase; 2) incongruent vaporization; 3) cluster vaporization. Second type is most wide spreader and character for chemically complicated minerals. As a rule in vapor phase the volatile oxides and their dissociation products are prevailed. The third type is least studied. We called it cluster type vaporization. It characterizes the vaporization of molecular blocks or large molecule and occurs at very high temperature and in condition of sharply temperature increase. The volatility of molecular blocks does not depend on the individual volatility of oxides and elements composing cluster. That is why the clusters can content the substances with different individual volatility that may lead to abundance of vapor by refractory elements. In the article there are number examples of cluster type vaporization. They are new experimental data of laser impulse vaporization of minerals such as larnite – $Ca_2[SiO_4]$, mervinite – $Ca_3Mg[SiO_4]_2$, plagioclase – An88 and wollastonite – $CaSiO_3$. The experiments showered that in vapor condensate, which was carried out from island silicates (larnite and mervinite), the silicates with chain connections are dominated and the molecular clusters with wollastonite and diopside chemical formula observed. The cluster vaporization mechanism may play important role (perhaps decisive role) in element distribution between vapor phase and remnant melt during impact processes. At these cases the use of classical row of oxide and element volatility for interpretation of the residual impact melt composition and the composition of condensate forms may lead to the erroneous conclusions.